

---

# Let the Target Select for Itself: Data Selection via Target-Aligned Paths

---

Huitao Yang Hengzhi He Guang Cheng  
University of California, Los Angeles  
{htyang03,hengzhihe,guangcheng}@ucla.edu

## Abstract

Targeted data selection aims to identify training samples from a large candidate pool that improve performance on a specific downstream task. Many recent methods estimate candidate utility by aggregating local attribution scores along a trajectory induced by the candidate pool. When the pool is heterogeneous, however, this reference trajectory may be misaligned with the dynamics of a target-aligned selected subset, creating what we call *reference path bias*. We propose an alternative reference path: a *validation-induced flow* obtained from a short, capacity-limited warmup on the available target validation proxy. Along this path, candidates are scored by a normalized endpoint loss drop, yielding a simple zero-order selection rule that requires no candidate gradients or Hessian approximations. Across controlled logistic, vision, and instruction-tuning experiments, this score is competitive with strong dynamic attribution baselines while substantially reducing warmup and storage cost. Moreover, since the reference trajectory is decoupled from any specific candidate pool, the same compact warmup can be reused across additional pools without recomputing the trajectory.

## 1 Introduction

Modern targeted data selection is increasingly shaped by a basic tension: high-quality attribution signals are expensive to collect, while cheap scores can miss the examples that matter for a target task. Given a large candidate pool and a small target validation set [49, 20, 19], influence-function scores provide a clean local objective but require inverse-Hessian information, while scalable trajectory methods replace this term with gradient alignments collected along training checkpoints:

$$I_{\text{IF}}(z) = \nabla_{\theta} R_{\text{val}}(\hat{\theta})^{\top} H_{\hat{\theta}}^{-1} \nabla_{\theta} \ell(\hat{\theta}; z), \quad I_{\text{path}}(z) = \sum_{t \in \mathcal{T}} \eta_t \langle \nabla_{\theta} R_{\text{val}}(\theta_t), \nabla_{\theta} \ell(\theta_t; z) \rangle. \quad (1)$$

Both scores use the “larger is better” utility convention here. Classical influence functions [21] instantiate the first score, whereas TracIn-style attribution and recent targeted-selection methods [34, 49, 18, 27] use variants of the second idea. This trajectory view removes the Hessian bottleneck, but it also makes the choice of reference path part of the compute–quality tradeoff. Adding checkpoints can improve a utility estimate only when those checkpoints lie on a path that is informative for the target; otherwise, extra trajectory compute can refine the wrong signal.

Figure 1 illustrates this failure mode. In a heterogeneous candidate pool, a reference trajectory induced by the raw pool can stay on a pool-dominated manifold while never visiting some regions on the target manifold. Examples from those regions may be useful after the model is moved toward the target, but they can look unimportant when their utility is measured only along the pool-induced path. The failure is therefore not merely selecting obviously bad examples; it is failing to expose potentially valuable data under the wrong reference trajectory. We refer to this failure mode as *reference-path bias*. The issue is not only how many checkpoints are collected, but whether the path used to collect them reveals candidate examples associated with the target manifold.

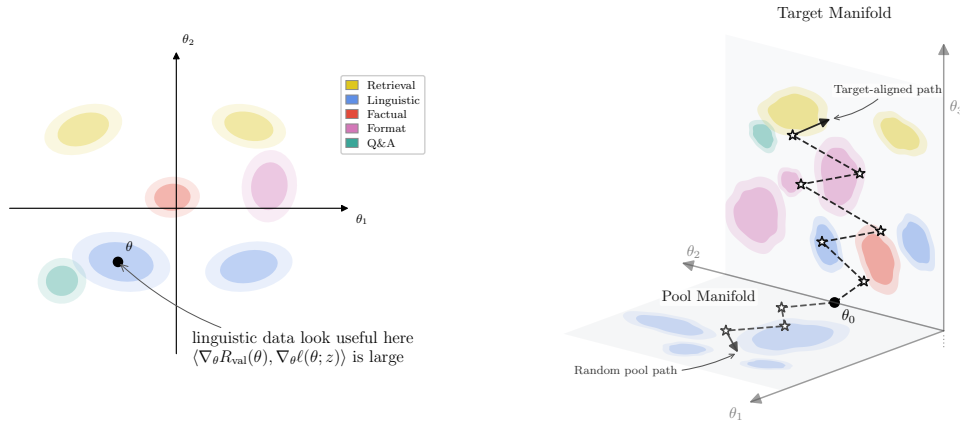


Figure 1: Conceptual illustration. **Left:** a 2D slice of parameter space; each colored region marks where that data type has high local alignment. **Right:** two possible reference trajectories on different manifolds. A pool-induced path can miss regions on the target manifold where some candidates become visible, even though those candidates may be valuable under a more target-aligned trajectory.

Motivated by this issue, we propose **Target-Aligned Candidate Selection (TACS)**, which replaces the pool-induced reference path with a lightweight trajectory induced by the target proxy. The core premise is that the best selected subset should train more like the target distribution than like the raw candidate pool. Instead of asking how candidates affect the target along a pool trajectory, TACS asks which candidates become easier as the model moves along the target-proxy path. This path inversion gives a simple forward-pass score while keeping trajectory construction independent of the candidate pool.

In summary, our framework aligns the optimization geometry of data attribution with the target task. Our core contributions are:

- **(I) A Trajectory Integral Perspective and Path Inversion:** We frame targeted data selection as a time integral along an optimization path and invert the standard approximation. By introducing the *Validation-Induced Flow*, we reduce dependence on pool-induced reference paths and bias the integration path toward the target proxy rather than heterogeneous pool dynamics.
- **(II) Zero-Order Scoring via Capacity Bottlenecks:** We provide an analytical interpretation, supported by empirical evidence, for using a candidate’s macroscopic loss drop along this target path as a simple zero-order proxy for downstream utility. To reduce rapid memorization on the small validation set, we use a *capacity bottleneck* during the warmup phase, which encourages the trajectory to capture broader target structure.
- **(III) Reusability and Pool-Independent Warmup:** This target-driven architecture supports a “compute-once, score-many” paradigm within a fixed model and target setup. Because the warmup path is generated independently of the candidate pool, the same compact trajectory can be reused to score additional candidate datasets with forward passes.

The rest of the paper is organized as follows. Section 2 positions TACS relative to targeted selection and gradient-matching methods; Sections 3 and 4 derive and instantiate the validation-induced scoring rule; Section 5 evaluates it across controlled prediction, vision, and instruction-tuning settings; and Section 6 summarizes the main theoretical scope.

## 2 Related Work

**Targeted Instruction-Data Selection.** The closest line of work selects instruction-tuning data for a specified downstream target using a small proxy set. LESS [49], ToV [18], and GIST [27] estimate target-aware utility from gradient, perturbation, or low-rank geometric signals. Other recent LLM selectors use mutual-information projection [10], proxy-label distribution matching [4],

reward or metric objectives [48, 43], and neuron-activation structure [46]. TACS addresses the same targeted-selection setting, but changes the reference path: it scores endpoint loss response along a target-induced trajectory rather than local utility along a pool-induced path.

**Data Attribution and Learning-Dynamics Signals.** Classical data-attribution methods estimate how examples affect model behavior through influence functions [21] or scalable trajectory approximations such as TracIn [34] and TRAK [31]. Separately, learning-dynamics methods use training behavior to diagnose example difficulty, learnability, or label quality [38, 32, 40, 33]. TACS also uses loss evolution as a utility signal, but evaluates it offline by forward passes through a short target-induced trajectory.

**Coresets, Gradient Matching, and Online Selection.** Coreset and gradient-matching methods select compact subsets whose gradients approximate a reference objective, including CRAIG [29], GradMatch [19], and GLISTER [20]. Recent dynamic selectors update data choices or weights during training, including optimizer-aware online selection [41], per-iteration pretraining selection [44], adaptive RL curricula [50], and bilevel influence learning such as BLISS [14]. This line of work supports the premise that useful subsets are not merely small or high-quality in isolation: they should induce updates aligned with the objective one ultimately cares about. TACS adopts this target-alignment view, but uses a target-proxy trajectory to expose candidate utility before subset retraining.

**Instruction-Data Quality and Capacity Control.** Instruction-tuning performance often depends more on data quality and task fit than on raw data volume alone [54, 2, 25, 52, 30, 53]. We use LoRA [17], motivated by the low intrinsic dimension of adaptation in large models [1], as a practical capacity bottleneck during the target warmup.

Appendix C provides a more detailed comparison with targeted selection, attribution, coreset, and instruction-data-quality methods.

## 3 Motivation

### 3.1 Problem Setting

We study the problem of targeted data selection: identifying a subset  $S \subseteq \mathcal{Z}_{\text{pool}}$  from a large, generic candidate pool  $\mathcal{Z}_{\text{pool}}$  that maximizes a model’s performance on a specific target task. Let  $\mathcal{D}$  denote the target distribution; Appendix D summarizes notation used throughout the paper. The goal is to choose  $S$  to minimize the expected target risk:

$$\min_{S \subseteq \mathcal{Z}_{\text{pool}}, |S| \leq N} R(\theta(S)) := \mathbb{E}_{z \sim \mathcal{D}} [\ell(\theta(S); z)], \quad (2)$$

where  $\theta(S) = \arg \min_{\theta \in \Theta} R_S(\theta) = \arg \min_{\theta \in \Theta} \frac{1}{|S|} \sum_{z \in S} \ell(\theta; z)$  is the trained model on  $S$ . Here,  $\ell$  is a smooth loss function and  $R_S$  denotes the empirical risk over  $S$ . In practice,  $\mathcal{D}$  is unavailable, and we rely on a small validation set  $\mathcal{Z}_{\text{val}}$  sampled from the target task as a proxy.

### 3.2 A Gradient Flow Formulation

To build intuition, suppose the model parameters  $\theta_t$  evolve according to the gradient flow induced by the selected subset  $S$ :

$$d\theta_t = -\eta_t \nabla R_S(\theta_t) dt. \quad (3)$$

By the chain rule, the evolution of the target risk  $R(\theta_t)$  along this trajectory is:

$$dR(\theta_t) = \langle \nabla R(\theta_t), d\theta_t \rangle = -\eta_t \langle \nabla R(\theta_t), \nabla R_S(\theta_t) \rangle dt. \quad (4)$$

Integrating from  $t = 0$  to  $T$  yields the macroscopic change in target risk:

$$R(\theta_T) - R(\theta_0) = - \int_0^T \eta_t \langle \nabla R(\theta_t), \nabla R_S(\theta_t) \rangle dt, \quad (5)$$

$$= - \frac{1}{|S|} \sum_{z \in S} \underbrace{\int_0^T \eta_t \langle \nabla R(\theta_t), \nabla \ell(\theta_t; z) \rangle dt}_{\text{Utility } F(z, \mathcal{T}=\{\theta_t\})} \quad (6)$$

Thus, conditional on a fixed trajectory  $\mathcal{T}$ , the target-risk reduction decomposes additively across examples. In the original problem, however,  $\mathcal{T}$  is itself induced by  $S$ , so each per-example utility remains coupled to all other selected examples through the shared trajectory.

Equation (5) therefore reveals that subset selection is naturally a coupled search over examples and the optimization trajectory they induce. We use this to lift the problem from searching only over subsets  $S$  to an augmented view over subset–trajectory pairs  $(S, \mathcal{T})$ , thereby making the optimization geometry an explicit component of candidate utility  $F(z; \mathcal{T})$ . Following the optimization principle of decoupling a hard joint search into easier subproblems [13, 35], if we have a rough estimate  $\hat{\mathcal{T}}$  of the trajectory induced by an optimal subset,  $\mathcal{T}(S^*)$ , we can replace  $\mathcal{T}$  by  $\hat{\mathcal{T}}$  and reduce the problem to a lower-dimensional selection problem over  $S$ .

**Reference Path Bias.** Existing attribution methods, such as LESS [49] and ToV [18], approximate this quantity along a *pool-induced trajectory*  $\theta_t^{\text{pool}}$ , where  $d\theta_t^{\text{pool}} = -\eta_t \nabla R_{\mathcal{Z}_{\text{pool}}}(\theta_t^{\text{pool}}) dt$ ; Appendix E gives the path-integral derivation and its connection to classical influence functions. However, when the candidate pool is heterogeneous and contains potentially irrelevant signals,  $\mathcal{T}^{\text{pool}} = \{\theta_t^{\text{pool}}\}$  may deviate from the trajectory induced by the selected subset. Candidate utility is then evaluated along such potentially misaligned trajectory, leading to a *reference path bias* (see Figure 1).

This raises a natural question:

*Can we construct a reference trajectory that better approximates the dynamics induced by the optimal subset?*

### 3.3 The Validation-Induced Flow

**Core idea.** The optimal subset  $S^*$  from a heterogeneous candidate pool should induce training dynamics closer to the target task than to the raw pool. In optimization terms, training on  $S^*$  should move parameters in directions similar to training on the target task itself. This assumption forms the theoretical bedrock of gradient-matching, coreset, and targeted selection literature [19, 29, 41, 28], which posits that a selected subset is optimal when its gradient vector field directionally aligns with the target’s vector field:

$$\nabla R_{S^*}(\theta) \approx \nabla R(\theta). \tag{7}$$

Because the true target risk  $R$  is inaccessible in practice, we approximate its geometry using the available target proxy,  $R_{\text{val}}$ . Rather than relying on a noisy, pool-induced path to accidentally overlap with this target geometry, we actively construct a *validation-induced flow*  $\theta_t^{\text{val}}$  by training exclusively on  $\mathcal{Z}_{\text{val}}$ :

$$d\theta_t^{\text{val}} = -\eta_t \nabla R_{\text{val}}(\theta_t^{\text{val}}) dt. \tag{8}$$

Because  $\mathcal{Z}_{\text{val}}$  isolates the target signal,  $\theta_t^{\text{val}}$  serves as a target-conditioned rough estimate of the optimal retraining dynamics  $\mathcal{T}(S^*)$ . As illustrated in Figure 2, this validation flow structurally matches the eventual selected-subset retraining dynamics far better than a generic pool path. We therefore utilize this validation-induced path as a heuristic geometric anchor for the time-integral estimate, rather than as a strict claim about the exact optimal retraining trajectory. We explicitly define the boundary conditions of this assumption in Section A.

## 4 Methodology

TACS turns the geometric argument in Section 3 into a deliberately simple selection rule. The central move is to reverse the usual attribution direction: instead of asking how each candidate changes target performance along a pool-trained path, we first let the target proxy define the path, then ask which candidates become easier under that target movement. This yields a three-stage pipeline: (1) learn a compact validation-induced trajectory, (2) score every candidate by its loss evolution along this fixed path, and (3) select the highest-scoring examples. Algorithm 1 summarizes the procedure.

---

**Algorithm 1** Target-Aligned Candidate Selection (TACS).

---

- 1: **Input:** Val set  $\mathcal{Z}_{\text{val}}$ , Pool  $\mathcal{Z}_{\text{pool}}$ , Budget  $N$
  - 2: **Initialize:** Base parameters  $\theta_0$
  - 3: Select learning rate  $\eta$  and epochs  $T$  via cross-validation (App. F.6)
  - 4: Generate target-aligned warmup trajectory on  $\mathcal{Z}_{\text{val}}$ ,  $\mathcal{T}_{\text{val}} = \{\theta_0^{\text{val}}, \dots, \theta_T^{\text{val}}\}$ , via Eq. 9
  - 5: **for** each candidate  $z \in \mathcal{Z}_{\text{pool}}$  **do**
  - 6:   Compute normalized candidate score  $s(z)$  via Eq. 16
  - 7: **end for**
  - 8: **return** Subset  $S \subset \mathcal{Z}_{\text{pool}}$  maximizing total score (Eq. 17)
- 

#### 4.1 Validation-Induced Trajectory

The only training step in TACS is a short warmup on the target validation set  $\mathcal{Z}_{\text{val}}$ . Starting from the base model  $\theta_0$ , we update parameters by gradient descent on validation risk:

$$\theta_t = \theta_{t-1} - \eta \nabla_{\theta} R_{\text{val}}(\theta_{t-1}), \quad R_{\text{val}}(\theta) = \frac{1}{|\mathcal{Z}_{\text{val}}|} \sum_{z \in \mathcal{Z}_{\text{val}}} \ell(\theta; z). \quad (9)$$

This produces the path  $\mathcal{T}_{\text{val}} = \{\theta_0^{\text{val}}, \dots, \theta_T^{\text{val}}\}$ . Importantly, the path is constructed without looking at  $\mathcal{Z}_{\text{pool}}$ . The same warmup can therefore be reused for any candidate pool that will later be scored against the same target task and base model.

**Structural Regularization via LoRA.** For microscopic validation sets, a validation-induced path is useful only if it captures task structure rather than memorizing a tiny validation set. We therefore construct the path through a strict Low-Rank Adaptation (LoRA) bottleneck [17]. In instruction-tuning experiments, we use ultra-low-rank adapters (e.g., rank  $r = 1$ ), forcing the warmup to express broad directions of target adaptation instead of high-capacity instance fitting. This bottleneck also makes the saved checkpoints lightweight, enabling cheap offline storage of trajectories.

**Trajectory Calibration.** We calibrate the learning rate  $\eta$  and trajectory length  $T$  using an  $M$ -fold cross-validation heuristic on  $\mathcal{Z}_{\text{val}}$ . For each candidate configuration, the remaining folds generate the warmup path, and the held-out fold is treated as target-like data to be separated from a small generic negative reference sample. This negative sample need not be drawn from the candidate pool later being scored. We choose  $(\eta^*, T^*)$  by maximizing rank-based AUROC between these two groups. This calibration favors trajectories whose loss-drop signal transfers across validation folds, rather than trajectories that only fit the examples used to construct the path. Full details are in Appendix F.6.

#### 4.2 Inverse Selection via Loss Evolution

For the continuous-time validation warmup,

$$\frac{d\theta_t^{\text{val}}}{dt} = -\eta_t \nabla R_{\text{val}}(\theta_t^{\text{val}}). \quad (10)$$

By the chain rule, the endpoint loss drop of a candidate along this path is exactly the accumulated alignment between the candidate gradient and the validation update direction:

$$\ell(\theta_0^{\text{val}}; z) - \ell(\theta_T^{\text{val}}; z) = \int_0^T \eta_t \langle \nabla \ell(\theta_t^{\text{val}}; z), \nabla R_{\text{val}}(\theta_t^{\text{val}}) \rangle dt. \quad (11)$$

Thus, if  $\mathcal{Z}_{\text{val}}$  is a faithful proxy for the target task ( $\nabla R_{\text{val}} \approx \nabla R$ ), the average loss drop over any selected subset  $S$  approximates the target-aligned integral from Section 3:

$$R_S(\theta_0^{\text{val}}) - R_S(\theta_T^{\text{val}}) \approx \frac{1}{|S|} \sum_{z \in S} \int_0^T \eta_t \langle \nabla \ell(\theta_t^{\text{val}}; z), \nabla R(\theta_t^{\text{val}}) \rangle dt \quad (12)$$

$$= \frac{1}{|S|} \sum_{z \in S} F(z, \mathcal{T} = \{\theta_t^{\text{val}}\}). \quad (13)$$

Under the two approximations above—the validation flow is a rough estimate of  $\mathcal{T}(S^*)$ , and the validation gradient estimates the target gradient—the macroscopic loss drop along this path becomes a forward-only proxy for how well a candidate responds to target-task learning. Operationally, this is the same quantity used to evaluate whether the retrained model has improved on the target proxy, applied in reverse to candidate examples. We therefore select candidates whose losses decrease most along the validation-induced path.

### 4.3 Candidate Scoring and Selection

Thus, we first measure the raw loss reduction each candidate experiences along the validation-induced trajectory:

$$\Delta\ell(z) = \ell(\theta_1^{\text{val}}; z) - \ell(\theta_T^{\text{val}}; z). \quad (14)$$

We use  $\theta_1^{\text{val}}$  rather than  $\theta_0^{\text{val}}$  as the baseline because the first update can be dominated by task-agnostic effects such as formatting adaptation and simple pattern learning [12]. Dropping this first step focuses the score on the more target-conditioned part of the path.

For token-level objectives (e.g., LLM SFT), prompt tokens are masked and the sample loss is averaged over response-token positions  $\mathcal{A}(z)$ :

$$\ell(\theta; z) = \frac{1}{|\mathcal{A}(z)|} \sum_{i \in \mathcal{A}(z)} -\log p(z_i | z_{<i}; \theta). \quad (15)$$

Longer sequences can have systematically different token-level losses, so raw loss drops may introduce length bias [49, 42, 48]. Figure 9 in the appendix provides a length diagnostic for the normalized score. We therefore use the relative loss reduction:

$$s(z) = \frac{\ell(\theta_1^{\text{val}}; z) - \ell(\theta_T^{\text{val}}; z)}{\max\{\ell(\theta_1^{\text{val}}; z), \varepsilon\}}. \quad (16)$$

Finally, we select the top- $N$  candidates:

$$S^* = \arg \max_{S \subseteq \mathcal{Z}_{\text{pool}}, |S|=N} \sum_{z \in S} s(z). \quad (17)$$

Many recent selection pipelines incorporate diversity, coverage, or deduplication constraints during the final sampling stage [10, 29, 20]. We use strict top- $N$  selection to isolate the effect of the scoring metric and maintain a fair comparison with attribution baselines under the same budget. More sophisticated sampling strategies, as well as alternative candidate metrics, can be applied on top of the same validation warmup when diversity control or task-specific scoring is desired. All candidates are evaluated by forward passes through the same two saved checkpoints, so selection cost scales with scoring the pool but the warmup cost is independent of the pool size.

## 5 Empirical Study

In this section, we evaluate TACS from controlled prediction tasks to instruction tuning. Full experimental settings are in Appendix F.

### 5.1 Controlled Prediction Tasks

**Toy Logistic Mixture.** We first study a controlled logistic mixture with known target and distractor components. Figure 2 shows that TACS-selected subsets induce retraining trajectories closer to the validation-warmup path than to the noisy pool-warmup path. This path alignment is associated with lower target classification error than LESS and ToV in this setting.

**Vision Selection Is Robust under Noisy Candidate Pools.** We next test TACS on binary CIFAR-10 target selection using an ImageNet-pretrained ResNet-18. The validation proxy contains 100 clean target samples, and the 10,000-image candidate pool is either clean or corrupted with 40% label noise. After selecting  $k$  examples, we evaluate downstream retraining under both full fine-tuning, which updates all model parameters, and partial fine-tuning, which updates only the classification

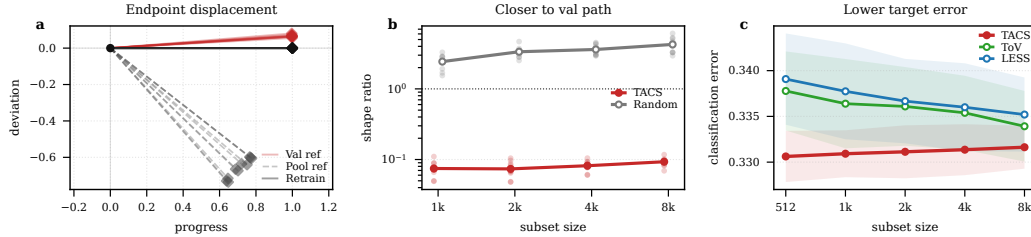


Figure 2: Toy logistic mixture. **(a)** Endpoint displacement directions for retraining, validation, and pool warmups projected to the 2D plane spanned by final retraining and validation displacements. **(b)** Shape-distance ratio; below 1 means retraining is closer to the validation path. **(c)** Better path alignment tracks lower target error.

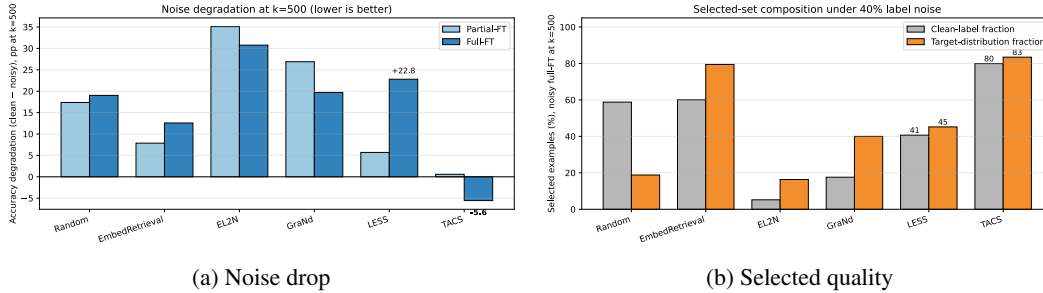


Figure 3: Binary CIFAR-10 selection with ResNet-18. Full FT updates all parameters; partial FT updates layer4+head. **(a)** Accuracy drop from clean to noisy pools at  $k = 500$  (lower is better). **(b)** Clean-label and target fractions under 40% label noise (higher is better).

head. At  $k = 500$ , LESS performs better in the clean full-finetuning setting, but degrades sharply under label noise, while TACS retains substantially higher accuracy. Figure 3 suggests that this robustness is associated with selected-set quality: under noise, TACS selects a much larger fraction of clean-label and target-distribution examples than LESS. Thus, the validation-induced trajectory acts as a task-conditioned filter rather than only selecting high-loss or high-gradient examples.

## 5.2 Instruction Tuning

We evaluate targeted data selection for instruction tuning with Llama-3.2-3B on MMLU, BBH, and TyDiQA. Each task’s development set is used as the validation proxy, while final performance is measured on the held-out test set. We select fixed-size subsets from Flan V2, Oasst1, COT, and Dolly, giving a cross-distribution setting where candidate pools may differ from the target task. For baselines, we compare with random selection and two dynamic attribution methods, LESS [49] and ToV [18].

**TACS Is Competitive across Heterogeneous Candidate Pools.** Table 1 shows that TACS improves over random selection in every instruction-tuning cell and obtains the best average result on all three target tasks. These gains are not uniform: LESS and ToV remain stronger in several MMLU and BBH cells. The most consistent gains appear on TyDiQA, suggesting that the validation-induced path can provide a useful target-conditioned scoring signal under pool-target mismatch. Since this path is constructed from the target proxy rather than from a specific candidate pool, it can be reused across candidate sources under a fixed model, target task, and scoring configuration.

**TACS Drastically Reduces Computational and Storage Overhead.** By fundamentally shifting warmup complexity from the candidate pool ( $\mathcal{O}(|\mathcal{Z}|)$ ) to the validation proxy ( $\mathcal{O}(|\mathcal{Z}_{\text{val}}|)$ ), TACS slashes measured warmup from hours to under one minute. Utilizing ultra-low capacity adapters ( $r = 1$ ) and eliminating gradient caching drops peak storage by four orders of magnitude—from 100 GB (LESS) to  $< 10$  MB. Because scoring requires only inexpensive forward passes at trajectory endpoints, evaluation is  $7\times$  faster than LESS and  $4\times$  faster than ToV. Finally, the 1.2-hour one-time

Table 1: PER-SOURCE INSTRUCTION-TUNING RESULTS. Best/second-best are **bold/underlined**; parentheses show gains over Random. Results are three-seed means, with SDs reported for LESS, ToV, and TACS.

Pool	Random			LESS			ToV			TACS (Ours)		
	MMLU	TyDiQA	BBH	MMLU	TyDiQA	BBH	MMLU	TyDiQA	BBH	MMLU	TyDiQA	BBH
COT	52.36	56.80	45.09	56.48 $\pm$ 0.6 (+4.12)	62.54 $\pm$ 1.2 (+5.74)	48.40 $\pm$ 1.6 (+3.31)	57.21 $\pm$ 0.8 (+4.85)	63.97 $\pm$ 0.5 (+7.17)	47.25 $\pm$ 0.8 (+2.16)	<b>57.22</b> $\pm$ 0.5 (+4.86)	<b>64.96</b> $\pm$ 1.7 (+8.16)	<b>49.44</b> $\pm$ 1.4 (+4.35)
Dolly	56.25	50.44	46.02	<u>59.37</u> $\pm$ 0.2 (+3.12)	59.10 $\pm$ 2.4 (+8.66)	<b>48.24</b> $\pm$ 1.1 (+2.22)	<u>59.30</u> $\pm$ 0.1 (+3.05)	<u>65.40</u> $\pm$ 0.8 (+14.96)	47.28 $\pm$ 0.3 (+1.26)	59.26 $\pm$ 0.3 (+3.01)	<b>66.59</b> $\pm$ 1.8 (+16.15)	<u>48.06</u> $\pm$ 0.3 (+1.63)
Flan	55.75	59.38	45.83	<u>56.93</u> $\pm$ 0.4 (+1.18)	61.60 $\pm$ 1.6 (+2.22)	47.04 $\pm$ 1.3 (+1.21)	55.98 $\pm$ 1.1 (+0.23)	<u>66.78</u> $\pm$ 0.4 (+7.40)	<u>47.62</u> $\pm$ 1.0 (+1.79)	<b>58.04</b> $\pm$ 0.9 (+2.29)	<b>67.41</b> $\pm$ 1.8 (+8.03)	<b>48.92</b> $\pm$ 0.3 (+3.09)
Oasst	56.19	35.15	46.11	<u>58.92</u> $\pm$ 0.1 (+2.73)	51.37 $\pm$ 2.9 (+16.22)	46.30 $\pm$ 1.8 (+0.19)	<b>59.37</b> $\pm$ 0.2 (+3.18)	<u>55.67</u> $\pm$ 2.3 (+20.52)	<u>48.06</u> $\pm$ 1.1 (+1.95)	58.52 $\pm$ 0.4 (+2.33)	<b>58.03</b> $\pm$ 1.8 (+22.88)	<b>49.38</b> $\pm$ 1.2 (+3.27)
Average	55.14	50.44	45.76	57.92 $\pm$ 0.1 (+2.78)	58.65 $\pm$ 0.7 (+8.21)	47.49 $\pm$ 0.8 (+1.73)	<u>57.96</u> $\pm$ 0.4 (+2.82)	<u>62.95</u> $\pm$ 0.7 (+12.51)	<u>47.55</u> $\pm$ 0.3 (+1.79)	<b>58.26</b> $\pm$ 0.3 (+3.12)	<b>64.25</b> $\pm$ 0.9 (+13.81)	<b>48.95</b> $\pm$ 0.5 (+3.19)

Table 2: **Empirical Efficiency Comparison.** Runtime is measured in single H200 GPU hours for Llama-3.2-3B across 4 sources and 3 tasks.  $d_f, d_b$  are forward/backward costs.  $d_{\text{proj}}$  is the gradient projection dimension. Calibration is the one-time hyperparameter search.

Method	Metric	Calibration	Warmup (total)	Scoring (total)	Total Peak Storage
LESS	Measured	–	2.7 h	24.0 h	100.0 GB
	Compl.	–	$\mathcal{O}(T \mathcal{Z} d_b)$	$\mathcal{O}(K \mathcal{Z} d_b)$	$\mathcal{O}(K \mathcal{Z} d_{\text{proj}} + K \dim(\phi_{128}))$
ToV	Measured	–	2.7 h	13.5 h	2.5 GB
	Compl.	–	$\mathcal{O}(T \mathcal{Z} d_b)$	$\mathcal{O}(2K \mathcal{Z} d_f)$	$\mathcal{O}(2K \mathcal{Z}  + 2K \dim(\phi_{128}))$
TACS	Measured	<b>1.2 h</b>	< 1 m	<b>3.3 h</b>	< 10 MB
	Compl.	–	$\mathcal{O}(T \mathcal{Z}_{\text{val}} d_b)$	$\mathcal{O}(2 \mathcal{Z} d_f)$	$\mathcal{O}(2 \mathcal{Z}  + 2 \dim(\phi_1))$

calibration overhead is rapidly amortized by the trajectory’s universal reusability across candidate pools.

### 5.2.1 Ablation Studies

**Low-Capacity Warmup Stabilizes Scores at a Potential Cost.** Figure 4a studies the effect of the LoRA rank used during the validation warmup. In our setting, the rank-one warmup gives the strongest and most stable selection signal. This is consistent with the role of the validation warmup as a low-capacity probe: since the target proxy is small, larger ranks can make the trajectory more sensitive to idiosyncratic validation examples rather than exposing a more transferable target direction. Increasing the rank therefore adds expressivity, but does not yield a consistent downstream improvement in this experiment.

**More Warmup Epochs Improve Selection Quality.** Figure 4b evaluates how the number of validation-warmup epochs affects candidate scoring. Short warmups provide only a weak target-conditioned signal, while more epochs allow the model to move further along the target-induced path. Over the tested range, downstream performance improves with the number of warmup epochs, suggesting that TACS benefits from observing a more developed target trajectory.

**Trajectory Scoring Is Not Just an Initial-Gradient Proxy.** Figure 4c compares TACS with a first-order perturbation score computed at the base model,  $\langle \nabla R_{\text{val}}(\theta_0), \nabla_{\theta} \ell(\theta_0; z) \rangle$ . The two methods select substantially different examples, and trajectory-based scoring achieves stronger downstream performance in this setting. This indicates that TACS is not simply approximating an initial-gradient baseline; its signal depends on how candidate losses evolve after the model moves along the target-induced path.

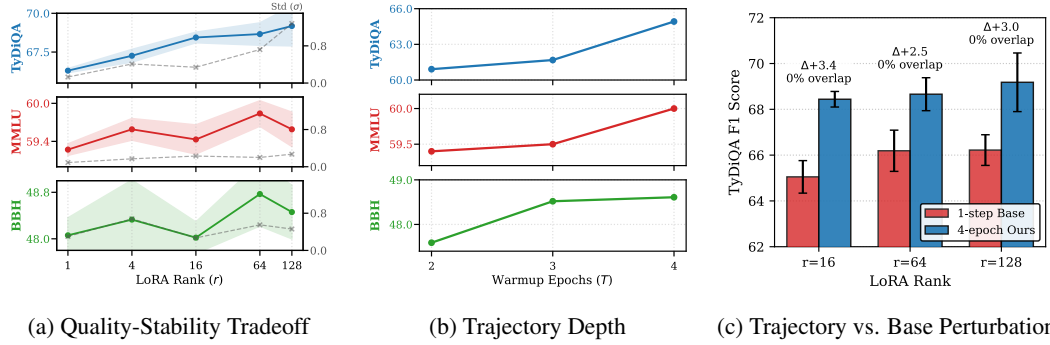


Figure 4: TyDiQA ablations. **(a)** Warmup rank controls the quality-stability tradeoff. **(b)** More warmup epochs improve selection. **(c)** Trajectory scoring outperforms a base-model perturbation score. Uncertainty is over warmup seeds only.

## 6 Discussion

### 6.1 Scope and Theoretical Justification

The scope of TACS depends on when an *inverse* signal—candidate loss reduction along a target-induced trajectory—transfers to the downstream objective. The informal bound below shows that transfer is controlled by closeness between the selected-subset and target distributions.

**Theorem 6.1** (Cross-Distribution Risk Bound, Informal). Let  $P_{\text{tar}}$  be the target distribution and let  $P_S$  be the distribution induced by a selected subset. Define the source-side improvement  $\Delta(S) := R_{P_S}(\theta_0) - R_{P_S}(\theta_{P_{\text{tar}}^*})$ . Under the convexity, smoothness, and data-Lipschitz conditions stated in Appendix E.5, there exist constants  $C_1, C_2 > 0$  such that

$$R_{P_{\text{tar}}}(\theta_0) - R_{P_{\text{tar}}}(\theta_{P_S}^*) \geq \Delta(S) - C_1 W_1(P_S, P_{\text{tar}}) - C_2 W_1(P_S, P_{\text{tar}})^2. \quad (18)$$

The main implication is that the inverse loss-drop signal is useful when high-scoring subsets also induce a distribution close to the target task. In this regime, increasing  $\Delta(S)$  can translate into downstream target improvement, up to a distribution-shift penalty. Conversely, when useful subsets must draw heavily from far-from-target regions, the Wasserstein terms can dominate the bound, and a large inverse loss drop need not imply downstream gain.

This suggests three practical scope conditions for TACS. First, the candidate pool should be sufficiently diverse and high quality so that a target-close useful subset exists; the selection budget should also remain moderate, since large budgets can force the selected distribution away from the target. Second, the target-induced warmup should produce a meaningful movement in parameter space. If the trajectory is nearly microscopic, reference-path bias becomes less important, and selection quality may be dominated instead by static data representations. Third, TACS is most relevant when the target distribution differs from the candidate-pool distribution; when they are already well aligned, the reference-path bias that TACS aims to correct is less significant. We defer the formal statement, proof, and further discussion of boundary conditions to Appendix E.

### 6.2 Conclusion

We identify the reference trajectory as an important design choice in targeted data selection and propose TACS, a lightweight target-proxy trajectory for reusable endpoint-loss scoring. Our results suggest that deliberately designed reference paths can make data selection more robust and scalable under pool heterogeneity.

## References

- [1] Armen Aghajanyan, Luke Zettlemoyer, and Sonal Gupta. Intrinsic dimensionality explains the effectiveness of language model fine-tuning, 2020. URL <https://arxiv.org/abs/2012.13255>.

- [2] Lichang Chen, Shiyang Li, Jun Yan, Hai Wang, Kalpa Gunaratna, Vikas Yadav, Zheng Tang, Vijay Srinivasan, Tianyi Zhou, Heng Huang, and Hongxia Jin. Alpapasus: Training a better alpaca with fewer data, 2024. URL <https://arxiv.org/abs/2307.08701>.
- [3] Sirui Chen, Yunzhe Qi, Mengting Ai, Yifan Sun, Ruizhong Qiu, Jiaru Zou, and Jingrui He. Influence-preserving proxies for gradient-based data selection in llm fine-tuning, 2026. URL <https://arxiv.org/abs/2602.17835>.
- [4] Hao Cheng, Rui Zhang, Ling Li, Na Di, Jiaheng Wei, Zhaowei Zhu, and Bo Han. Task-aware data selection via proxy-label enhanced distribution matching for LLM finetuning. In *The Fourteenth International Conference on Learning Representations*, 2026. URL <https://openreview.net/forum?id=R40WoYbYab>.
- [5] Jonathan H Clark, Eunsol Choi, Michael Collins, Dan Garrette, Tom Kwiatkowski, Vitaly Nikolaev, and Jennimaria Palomaki. TyDi QA: A benchmark for information-seeking question answering in typologically diverse languages. *Transactions of the Association for Computational Linguistics*, 8:454–470, 2020.
- [6] Mike Conover, Matt Hayes, Ankit Mathur, Jianwei Xie, Jun Wan, Sam Shah, Ali Ghodsi, Patrick Wendell, Matei Zaharia, and Reynold Xin. Free Dolly: Introducing the world’s first truly open instruction-tuned LLM. <https://www.databricks.com/blog/2023/04/12/dolly-first-open-commercially-viable-instruction-tuned-llm>, Apr 2023. Databricks Blog.
- [7] David R. Cox. The regression analysis of binary sequences. *Journal of the Royal Statistical Society: Series B*, 20(2):215–242, 1958.
- [8] Jia Deng, Wei Dong, Richard Socher, Li-Jia Li, Kai Li, and Li Fei-Fei. Imagenet: A large-scale hierarchical image database. In *Proceedings of the IEEE Conference on Computer Vision and Pattern Recognition*, pages 248–255, 2009.
- [9] Zhiwei Deng, Tao Li, and Yang Li. Influential language data selection via gradient trajectory pursuit, 2024. URL <https://arxiv.org/abs/2410.16710>.
- [10] Victor Ye Dong, Kuan-Yun Lee, Jiamei Shuai, Shen Liu, Yi Liu, and Jian Jiao. Greedy information projection for llm data selection. arXiv, March 2026. URL <https://www.microsoft.com/en-us/research/publication/greedy-information-projection-for-llm-data-selection/>.
- [11] Abhimanyu Dubey, Abhinav Jauhri, Abhinav Pandey, Abhishek Kadian, Ahmad Al-Dahle, Aiesha Letman, Akhil Mathur, Alan Schelten, Amy Yang, Angela Fan, et al. The llama 3 herd of models. *arXiv preprint arXiv:2407.21783*, 2024.
- [12] Jonathan Frankle, David J. Schwab, and Ari S. Morcos. The early phase of neural network training, 2020. URL <https://arxiv.org/abs/2002.10365>.
- [13] Gene H. Golub and Victor Pereyra. The differentiation of pseudo-inverses and nonlinear least squares problems whose variables separate. *SIAM Journal on Numerical Analysis*, 10(2): 413–432, 1973. doi: 10.1137/0710036.
- [14] Jie Hao, Rui Yu, Wei Zhang, Huixia Wang, Jie Xu, and Mingrui Liu. Bliss: A lightweight bilevel influence scoring method for data selection in language model pretraining, 2026. URL <https://arxiv.org/abs/2510.06048>.
- [15] Kaiming He, Xiangyu Zhang, Shaoqing Ren, and Jian Sun. Deep residual learning for image recognition. In *Proceedings of the IEEE Conference on Computer Vision and Pattern Recognition*, pages 770–778, 2016.
- [16] Dan Hendrycks, Collin Burns, Steven Basart, Andy Zou, Mantas Mazeika, Dawn Song, and Jacob Steinhardt. Measuring massive multitask language understanding. In *Proceedings of the International Conference on Learning Representations (ICLR)*, 2021.

- [17] Edward J. Hu, Yelong Shen, Phillip Wallis, Zeyuan Allen-Zhu, Yuanzhi Li, Shean Wang, Lu Wang, and Weizhu Chen. Lora: Low-rank adaptation of large language models, 2021. URL <https://arxiv.org/abs/2106.09685>.
- [18] Ayush Jain, Andrea Montanari, and Eren Sasoglu. Train on validation (tov): Fast data selection with applications to fine-tuning, 2025. URL <https://arxiv.org/abs/2510.00386>.
- [19] Krishnateja Killamsetty, Durga Sivasubramanian, Ganesh Ramakrishnan, Abir De, and Rishabh Iyer. Grad-match: Gradient matching based data subset selection for efficient deep model training, 2021. URL <https://arxiv.org/abs/2103.00123>.
- [20] Krishnateja Killamsetty, Durga Sivasubramanian, Ganesh Ramakrishnan, and Rishabh Iyer. Glist: Generalization based data subset selection for efficient and robust learning, 2021. URL <https://arxiv.org/abs/2012.10630>.
- [21] Pang Wei Koh and Percy Liang. Understanding black-box predictions via influence functions. In Doina Precup and Yee Whye Teh, editors, *Proceedings of the 34th International Conference on Machine Learning*, volume 70 of *Proceedings of Machine Learning Research*, pages 1885–1894. PMLR, 06–11 Aug 2017. URL <https://proceedings.mlr.press/v70/koh17a.html>.
- [22] Ron Kohavi. A study of cross-validation and bootstrap for accuracy estimation and model selection. In *Proceedings of the 14th International Joint Conference on Artificial Intelligence*, pages 1137–1145, 1995.
- [23] Andreas Köpf, Yannic Kilcher, Dimitri von Rütte, Sotiris Anagnostidis, Zhi-Rui Tam, Keith Stevens, Abdullah Barhoum, Duc Nguyen, Oliver Stanley, Richárd Nagyfi, et al. Openassistant conversations—democratizing large language model alignment, 2023.
- [24] Alex Krizhevsky. Learning multiple layers of features from tiny images. Technical report, University of Toronto, 2009.
- [25] Wei Liu, Weihao Zeng, Keqing He, Yong Jiang, and Junxian He. What makes good data for alignment? a comprehensive study of automatic data selection in instruction tuning, 2024. URL <https://arxiv.org/abs/2312.15685>.
- [26] Shayne Longpre, Le Hou, Tu Vu, Albert Webson, Hyung Won Chung, Yi Tay, Denny Zhou, Quoc V Le, Barret Zoph, Jason Wei, and Adam Roberts. The flan collection: Designing data and methods for effective instruction tuning. In *Proceedings of the 40th International Conference on Machine Learning (ICML)*, pages 22631–22648, 2023.
- [27] Guanghui Min, Tianhao Huang, Ke Wan, and Chen Chen. Gist: Targeted data selection for instruction tuning via coupled optimization geometry, 2026. URL <https://arxiv.org/abs/2602.18584>.
- [28] Sören Mindermann, Jan M Brauner, Muhammed T Razzak, Mrinank Sharma, Andreas Kirsch, Winnie Xu, Benedikt Hölzgen, Aidan N Gomez, Adrien Morisot, Sebastian Farquhar, and Yarin Gal. Prioritized training on points that are learnable, worth learning, and not yet learnt. In Kamalika Chaudhuri, Stefanie Jegelka, Le Song, Csaba Szepesvari, Gang Niu, and Sivan Sabato, editors, *Proceedings of the 39th International Conference on Machine Learning*, volume 162 of *Proceedings of Machine Learning Research*, pages 15630–15649. PMLR, 17–23 Jul 2022. URL <https://proceedings.mlr.press/v162/mindermann22a.html>.
- [29] Baharan Mirzasoleiman, Jeff Bilmes, and Jure Leskovec. Coresets for data-efficient training of machine learning models, 2020. URL <https://arxiv.org/abs/1906.01827>.
- [30] Jinlong Pang, Na Di, Zhaowei Zhu, Jiaheng Wei, Hao Cheng, Chen Qian, and Yang Liu. Token cleaning: Fine-grained data selection for llm supervised fine-tuning. In *Proceedings of the 42nd International Conference on Machine Learning*, pages 47837–47858, 2025. URL <https://arxiv.org/abs/2502.01968>.
- [31] Sung Min Park, Kristian Georgiev, Andrew Ilyas, Guillaume Leclerc, and Aleksander Madry. Trak: Attributing model behavior at scale, 2023. URL <https://arxiv.org/abs/2303.14186>.

- [32] Mansheej Paul, Surya Ganguli, and Gintare Karolina Dziugaite. Deep learning on a data diet: Finding important examples early in training, 2023. URL <https://arxiv.org/abs/2107.07075>.
- [33] Geoff Pleiss, Tianyi Zhang, Ethan R. Elenberg, and Kilian Q. Weinberger. Identifying mislabeled data using the area under the margin ranking, 2020. URL <https://arxiv.org/abs/2001.10528>.
- [34] Garima Pruthi, Frederick Liu, Mukund Sundararajan, and Satyen Kale. Estimating training data influence by tracing gradient descent, 2020. URL <https://arxiv.org/abs/2002.08484>.
- [35] Meisam Razaviyayn, Mingyi Hong, and Zhi-Quan Luo. A unified convergence analysis of block successive minimization methods for nonsmooth optimization. *SIAM Journal on Optimization*, 23(2):1126–1153, 2013. doi: 10.1137/120891009.
- [36] Mervyn Stone. Cross-validators choice and assessment of statistical predictions. *Journal of the Royal Statistical Society: Series B*, 36(2):111–133, 1974.
- [37] Mirac Suzgun, Nathan Scales, Nathanael Schärli, Sebastian Gehrmann, Yi Tay, Hyung Won Chung, Aakanksha Chowdhery, Quoc V Le, Ed H Chi, Denny Zhou, et al. Challenging BIG-bench tasks and whether chain-of-thought can solve them. In *Findings of the Association for Computational Linguistics: ACL 2023*, pages 13003–13051, 2023.
- [38] Swabha Swayamdipta, Roy Schwartz, Nicholas Lourie, Yizhong Wang, Hannaneh Hajishirzi, Noah A. Smith, and Yejin Choi. Dataset cartography: Mapping and diagnosing datasets with training dynamics, 2020. URL <https://arxiv.org/abs/2009.10795>.
- [39] Naftali Tishby, Fernando C. Pereira, and William Bialek. The information bottleneck method, 2000. URL <https://arxiv.org/abs/physics/0004057>.
- [40] Mariya Toneva, Alessandro Sordani, Remi Tachet des Combes, Adam Trischler, Yoshua Bengio, and Geoffrey J. Gordon. An empirical study of example forgetting during deep neural network learning, 2019. URL <https://arxiv.org/abs/1812.05159>.
- [41] Fangxin Wang, Peyman Baghersahi, Langzhou He, Henry Peng Zou, Sourav Medya, and Philip S. Yu. Two-stage optimizer-aware online data selection for large language models, 2026. URL <https://arxiv.org/abs/2604.00001>.
- [42] Jiachen T. Wang, Tianji Yang, James Zou, Yongchan Kwon, and Ruoxi Jia. Rethinking data shapley for data selection tasks: Misleads and merits, 2024. URL <https://arxiv.org/abs/2405.03875>.
- [43] Jingtang Wang, Xiaoqiang Lin, Rui Qiao, Pang Wei Koh, Chuan-Sheng Foo, and Bryan Kian Hsiang Low. NICE data selection for instruction tuning in LLMs with non-differentiable evaluation metric. In *Forty-second International Conference on Machine Learning*, 2025. URL <https://openreview.net/forum?id=2wt8m5HUBs>.
- [44] Shaobo Wang, Xuan Ouyang, Tianyi Xu, Yuzheng Hu, Jialin Liu, Guo Chen, Tianyu Zhang, Junhao Zheng, Kexin Yang, Xingzhang Ren, Dayiheng Liu, and Linfeng Zhang. Opus: Towards efficient and principled data selection in large language model pre-training in every iteration, 2026. URL <https://arxiv.org/abs/2602.05400>.
- [45] Yizhong Wang, Hamish Ivison, Pradeep Dasigi, Jack Hessel, Tushar Khot, Khyathi Raghavi Chandu, David Wadden, Kelsey MacMillan, Noah A. Smith, Iz Beltagy, and Hannaneh Hajishirzi. How far can camels go? exploring the state of instruction tuning on open resources, 2023. URL <https://arxiv.org/abs/2306.04751>.
- [46] Zijun Wang, Haoqin Tu, Weidong Zhou, Yiyang Zhou, Xiaohuan Zhou, Bingni Zhang, Weiguo Feng, Taifeng Wang, Cihang Xie, and Fengze Liu. Target-oriented pretraining data selection via neuron-activated graph, 2026. URL <https://arxiv.org/abs/2604.15706>.
- [47] Jason Wei, Xuezhi Wang, Dale Schuurmans, Maarten Bosma, Brian Ichter, Fei Xia, Ed Chi, Quoc Le, and Denny Zhou. Chain-of-thought prompting elicits reasoning in large language models, 2023. URL <https://arxiv.org/abs/2201.11903>.

- [48] Yang Wu, Huayi Zhang, Yizheng Jiao, Lin Ma, Xiaozhong Liu, Jinhong Yu, Dongyu Zhang, Dezhi Yu, and Wei Xu. Rose: A reward-oriented data selection framework for llm task-specific instruction tuning, 2025. URL <https://arxiv.org/abs/2412.00631>.
- [49] Mengzhou Xia, Sadhika Malladi, Suchin Gururangan, Sanjeev Arora, and Danqi Chen. Less: Selecting influential data for targeted instruction tuning, 2024. URL <https://arxiv.org/abs/2402.04333>.
- [50] Ningyuan Yang, Weihua Du, Weiwei Sun, Sean Welleck, and Yiming Yang. Gradalign: Gradient-aligned data selection for llm reinforcement learning, 2026. URL <https://arxiv.org/abs/2602.21492>.
- [51] Bolin Zhang, Jiahao Wang, Qianlong Du, Jiajun Zhang, Zhiying Tu, and Dianhui Chu. A survey on data selection for llm instruction tuning. *Journal of Artificial Intelligence Research*, 83, August 2025. ISSN 1076-9757. doi: 10.1613/jair.1.17625. URL <http://dx.doi.org/10.1613/jair.1.17625>.
- [52] Dylan Zhang, Qirun Dai, and Hao Peng. The best instruction-tuning data are those that fit, 2025. URL <https://arxiv.org/abs/2502.04194>.
- [53] Zizhuo Zhang, Qizhou Wang, Shanshan Ye, Jianing Zhu, Jiangchao Yao, Bo Han, and Masashi Sugiyama. Towards understanding valuable preference data for large language model alignment, 2026. URL <https://arxiv.org/abs/2510.13212>.
- [54] Chunting Zhou, Pengfei Liu, Puxin Xu, Sridi Iyer, Jiao Sun, Yuning Mao, Xuezhe Ma, Avia Efrat, Ping Yu, Lili Yu, Susan Zhang, Gargi Ghosh, Mike Lewis, Luke Zettlemoyer, and Omer Levy. Lima: Less is more for alignment, 2023. URL <https://arxiv.org/abs/2305.11206>.

## A Limitations

While our target-aligned trajectory framework offers a highly scalable and modular approach to data selection, it operates under specific boundary conditions. We explicitly define these limitations below to clarify the scope, theoretical commitments, and empirical boundaries of our method.

### A.1 Dependence on Validation Proxy Fidelity

Our framework inherently assumes that the microscopic validation set  $\mathcal{Z}_{\text{val}}$  provides a geometrically faithful representation of the true downstream target distribution. If  $\mathcal{Z}_{\text{val}}$  is too small or noisy to express the primary structural features of the target task, the resulting validation-induced flow will deviate from the optimal task geometry. In such zero-shot or severely misaligned regimes, careful data curation or improved target-proxy construction must take precedence over attribution methodology.

### A.2 Capacity Bottlenecks and Hyperparameter Sensitivity

To prevent rapid memorization of the microscopic validation set, TACS relies on a capacity-limited warmup. While we employ LoRA as a highly effective, parameter-efficient capacity restrictor, the operative mechanism is the *bottleneck itself*, not an intrinsic property of LoRA. Consequently, the method introduces sensitivities to specific hyperparameters, notably the bottleneck rank, warmup duration, and validation set size. While our experiments establish robust default configurations across multiple domains, optimal tuning may vary depending on the scale and complexity of the target task. A comprehensive, large-scale sensitivity analysis of these parameters across diverse architectures remains an important direction for future work.

### A.3 The Theory-Practice Gap in LLM Attribution

Providing tight approximation bounds relative to ideal influence functions remains a notoriously open problem in non-convex optimization. Consequently, our theoretical discussion (Section 3) is not intended to provide a bounded approximation error for the complete, discrete training pipeline. Rather, we utilize continuous-time gradient flow to rigorously derive *why* our zero-order heuristic (endpoint loss drop) effectively isolates target-aligned geometry. We do not analyze the discrete retraining dynamics post-selection, including finite-step optimizer effects, minibatch noise, or adapter-to-full-model mismatch. The theory serves to explain the mechanism of the TACS signal, while our empirical sections validate its survival under actual discrete training procedures.

### A.4 Boundary Conditions for Pool Reusability

A key advantage of TACS is the  $\mathcal{O}(1)$  scalability achieved by decoupling the warmup trajectory from the candidate pool, allowing a single trajectory to be reused. However, this claim of computational reusability holds a fundamental geometric boundary condition (formalized in Theorem 6.1): the inverse scoring rule weakly transmits to downstream gains *only if* the diverse candidate pool actually contains a meaningful subset of target-aligned data. If an unseen candidate pool is entirely out-of-distribution (i.e., the Wasserstein distance to the target is exceptionally large), the optimal parameter movements may be largely orthogonal to the validation-induced path. The bound is also most meaningful when the selection budget is tight enough that targeted filtering matters. If the entire pool already closely matches the target, or if final optimization is nearly infinitesimal, endpoint loss drops may contain little information beyond local gradient alignment.

## B Broader Impacts

Targeted data selection can lower the compute and data cost of adapting general-purpose models, making fine-tuning more accessible and reducing energy use. It also yields a transparent record of which examples were judged useful for a given target. The method inherits the values of the validation proxy  $\mathcal{Z}_{\text{val}}$ : if the proxy encodes biased or harmful behavior, selection may reinforce it, and the same efficiency gains could be used for harmful adaptation such as disinformation or surveillance. We release no new pretrained model or scraped corpus. The natural mitigation is to treat the validation

proxy as a governance artifact by documenting its provenance and auditing selected subsets before retraining propagates fairness and safety constraints into the selected data.

### C Extended Related Work

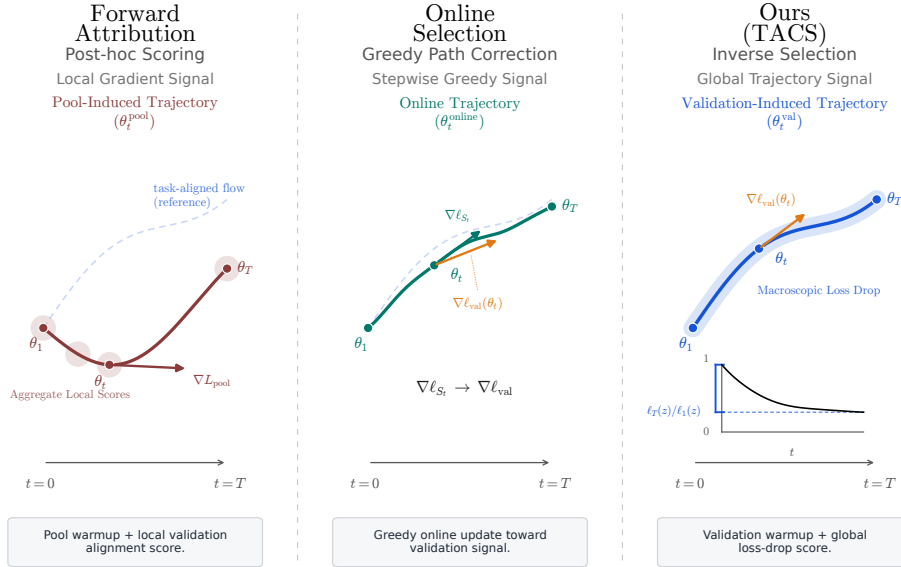


Figure 5: Dynamic selection paradigms: forward attribution along a pool path, online gradient matching, and TACS inverse selection along a validation-induced path.

Figure 5 situates TACS against the two adjacent paradigms that recur throughout this section: forward attribution along a pool-induced trajectory and online gradient matching. The discussion below uses the same partition—nearest local-attribution baselines, target-signal variants, online and bilevel selectors, and orthogonal data-quality methods—and identifies in each case which of the three regimes a method belongs to.

**Nearest Targeted Instruction-Selection Baselines.** The closest comparisons to TACS are local attribution methods that score instruction-tuning candidates using a target proxy or validation set, corresponding to the left panel of Figure 5. **LESS** [49] is the canonical baseline in this family: it computes validation-candidate gradient similarity along a warmup trajectory and aggregates the resulting local influence scores. **ToV** [18] is close to LESS in objective rather than a separate conceptual family. It targets the same validation-conditioned selection problem but uses perturbation-based approximations to reduce the cost of estimating the local train-validation effect. **GIST** [27] is also adjacent to LESS: it introduces a geometry-aware, local low-rank estimate of the same kind of validation-candidate attribution signal. In this view, LESS, ToV, and GIST differ mainly in how they estimate or compress local target-aware attribution.

TACS differs from this family at the level of the scoring signal. Rather than estimating a local gradient or perturbation score at many reference points, TACS first constructs a target-induced trajectory and then measures each candidate’s macroscopic endpoint loss drop along that path. The nearest-baseline question is therefore not only whether the attribution estimator is cheaper or lower rank, but whether candidate utility should be measured as a local validation-candidate interaction or as a zero-order response to target learning. This is also the main distinction from GIST: GIST uses low-rank geometry to estimate a local attribution score, whereas TACS uses a capacity-limited target trajectory to avoid local gradient scoring during pool evaluation.

Gradient-trajectory pursuit [9] is related in spirit because it treats language-data selection as a dynamic attribution problem. The difference again lies in where the trajectory comes from and what is stored.

TACS intentionally decouples the warmup from the candidate pool, which makes the same target trajectory reusable across candidate sources for a fixed base model and target proxy.

**Same Task, Different Target Signal.** A second group studies targeted or task-aware LLM data selection, but uses signals that are not direct substitutes for TACS. **GIP** [10] formulates selection through information projection onto task queries, emphasizing information coverage and diversity. This is target-aware, but its utility is information-theoretic rather than a response to target-induced learning. **Task-Aware Distribution Matching** [4] uses proxy labels to match the joint distribution of selected data to the target. This is closest to TACS at the problem level, but it operationalizes target alignment as distribution matching; TACS operationalizes alignment as loss reduction under a validation-induced trajectory. **NICE** [43] directly optimizes selection for non-differentiable evaluation metrics, and **ROSE** [48] uses reward-oriented signals for task-specific instruction tuning. These methods are metric- or reward-aware, whereas TACS is trajectory-aware: it does not require a task reward model or a differentiable surrogate for the final metric, only a small target proxy capable of inducing a useful warmup direction.

Training-free or weakly trained target-oriented methods occupy another adjacent but distinct space. **NAG-based ranking** [46] uses neuron-activation graph structure for target-oriented pretraining-data selection. Its appeal is that it avoids full retraining, but its setting and signal differ from TACS: NAG targets pretraining selection with neuron-centric structure, while TACS targets downstream instruction selection with a reusable validation-induced path. Fit-based data selection, including work arguing that strong instruction-tuning data are those that fit the target model [52], is conceptually close because it also emphasizes target-model compatibility. TACS differs by measuring compatibility after the model has moved in the target direction. In this sense, fit-based methods ask whether an example already fits the model or target model, while TACS asks whether the example responds to learning the target.

**Bilevel, Online, and Long-Horizon Selectors.** Influence functions [21], TracIn [34], and TRAK [31] connect example utility to gradients, Hessian structure, and training trajectories. These methods provide the conceptual basis for path-dependent attribution, but their direct application to modern LLM selection is often expensive. Optimizer-aware online data selection [41], OPUS [44], BLISS [14], and GradAlign [50] update or approximate utility during training. BLISS is especially relevant because it is validation-guided and bilevel in spirit, although it is positioned for pretraining rather than the few-shot targeted instruction-tuning regime studied here. GradAlign is also philosophically close because it uses a small trusted signal as a directional probe, but it studies RL fine-tuning rather than supervised instruction-data subset selection. TACS is offline after the target warmup: it borrows the idea that training dynamics expose utility, but avoids online selection loops, long-horizon bilevel optimization, and per-candidate gradient caching during scoring.

**Coresets and Gradient Matching.** CRAIG [29], GradMatch [19], and GLISTER [20] select subsets whose gradients approximate a full training or validation objective. These methods are important because they make the target-versus-pool distinction explicit: matching a pool statistic is not equivalent to following a target statistic when the pool is heterogeneous. TACS can be read as a zeroth-order, trajectory-level relaxation of target gradient matching. Instead of requiring explicit high-dimensional gradient matching at many candidate points, it uses the candidate’s loss footprint along a target-induced path as a proxy for whether the candidate agrees with the target vector field.

**Orthogonal Data-Quality and Fine-Grained Filtering.** Several works identify generally useful, learnable, clean, or high-quality data without necessarily solving the same targeted subset-selection problem. Dataset Cartography [38], forgetting events [40], mislabeled-data diagnostics [33], RHO-LOSS [28], and Data Diet/GraNd/EL2N-style pruning [32] show that early learning dynamics can identify easy, hard, noisy, or influential examples. These methods are useful baselines in controlled vision experiments, where generic data-pruning signals are natural competitors, but they are not nearest neighbors for TACS in targeted instruction tuning because they do not condition the selection signal on a target validation trajectory. Token Cleaning [30] operates at a finer granularity, removing or selecting tokens rather than choosing a subset of examples for a target task. It is therefore orthogonal: token-level quality control could potentially be applied before or after TACS, but it does not replace target-conditioned example selection.

**Instruction-Data Quality and Capacity Control.** LIMA [54], AlpaGasus [2], broad instruction-data quality analyses [25], fit-based studies [52], token-level cleaning [30], and preference-data analysis [53] support the broader view that data quality and target compatibility can matter more than raw data volume in some instruction-tuning regimes. TACS contributes a target-conditioned scoring mechanism for this regime. Separately, LoRA [17], intrinsic-dimensionality results [1], and information-bottleneck perspectives [39] motivate restricting the capacity of the validation warmup. In TACS, the low-rank adapter is not the theoretical object of interest; it is a practical bottleneck that prevents a very small validation proxy from being memorized too quickly and makes target checkpoints cheap to store and reuse.

Influence-preserving proxy methods such as IProX [3] are relevant to this implementation layer rather than to the main LESS/ToV/GIST comparison. IProX studies how to construct proxies that preserve gradient-based selection behavior while reducing cost. Such proxy or compression ideas could potentially be applied to the TACS warmup or capacity-restriction step, for example by improving the surrogate model or adapter used to generate the validation-induced path. This is complementary to our contribution: TACS changes the scoring signal to endpoint loss response, while IProX-style proxy design could be used to instantiate that path more efficiently or robustly. Recent surveys [51] provide a broader overview of LLM instruction-data selection beyond the targeted comparison emphasized here.

## D Notation Table

Table 3: Notation used throughout the paper. We reserve calligraphic  $\mathcal{Z}$  for finite datasets or pools and calligraphic  $\mathcal{D}$  for population distributions.

Symbol	Meaning
$\mathcal{Z}_{\text{pool}}$ or $\mathcal{Z}$	finite candidate pool from which examples are selected
$\mathcal{Z}_{\text{val}}$	finite target validation/proxy set used to construct the warmup trajectory
$\mathcal{D}, \mathcal{D}_{\text{tar}}$	target population distribution underlying $\mathcal{Z}_{\text{val}}$ and test data
$z$	one candidate or validation example; for SFT, an input-output sequence pair
$S \subseteq \mathcal{Z}_{\text{pool}}$	selected subset used for downstream retraining
$N$	selection budget, i.e., $ S  = N$
$\theta_0, \theta_t, \theta_T$	initial, intermediate, and final model parameters along a trajectory
$\theta_t^{\text{val}}, \theta_t^{\text{pool}}$	validation-induced and pool-induced trajectory states
$\mathcal{T} = \{\theta_t\}_{t=0}^T$	optimization trajectory used for attribution or scoring
$\eta_t$	learning rate or continuous-time step size at time $t$
$\ell(\theta; z)$	per-example loss of parameters $\theta$ on example $z$
$R(\theta), R_{\text{val}}(\theta), R_S(\theta)$	target, validation empirical, and selected-subset risks
$F(z, \mathcal{T})$	path-integrated alignment utility of candidate $z$ along $\mathcal{T}$
$\Delta\ell(z)$	endpoint loss drop $\ell(\theta_1^{\text{val}}; z) - \ell(\theta_T^{\text{val}}; z)$
$s(z)$	normalized TACS score, $\Delta\ell(z) / \max\{\ell(\theta_1^{\text{val}}; z), \varepsilon\}$
$r, \alpha$	LoRA rank and scaling factor used in adapter warmups
$M, K$	number of cross-validation folds and trajectory-depth candidates
$W_1(\cdot, \cdot)$	Wasserstein-1 distance used in the transfer bound

## E Omitted Theory: Influence as a Path Integral

This appendix formalizes the path-integral view introduced in the main text. Rather than providing a complete theory of discrete fine-tuning, our goal is to mathematically isolate the source of *reference-path bias* and demonstrate why classical influence functions fail to capture finite-time, early-stopping dynamics.

### E.1 Trajectory-Based Attribution

Let  $R_0$  be a reference objective that generates a training trajectory, and  $R$  be the target objective. Consider the learning-rate weighted gradient-flow trajectory:

$$\frac{d\theta_t}{dt} = -\eta_t \nabla R_0(\theta_t), \quad \theta_0 \text{ fixed}, \quad (19)$$

where  $\eta_t \geq 0$ . For a candidate example  $z$ , we define the finite-time trajectory score as the continuous-time analogue of discrete attribution methods (e.g., TracIn, LESS):

$$\mathcal{I}_{R,R_0}^T(z) := \int_0^T \eta_t \langle \nabla R(\theta_t), \nabla_{\theta} \ell(\theta_t; z) \rangle dt. \quad (20)$$

**Lemma E.1** (Discrete-to-continuous limit). Suppose reference checkpoints are generated by  $\theta_{t+1} = \theta_t - \eta_t \nabla R_0(\theta_t)$ , and the step sizes define a vanishing mesh over  $[0, T]$ . Under standard smoothness assumptions, the weighted discrete score  $\sum_t \eta_t \langle \nabla R(\theta_t), \nabla_{\theta} \ell(\theta_t; z) \rangle$  converges to  $\mathcal{I}_{R,R_0}^T(z)$ .

Equation (20) explicitly separates two roles: the target  $R$  determines the vector field, while the reference  $R_0$  determines *where* in parameter space this field is evaluated. Changing  $R_0$  inherently changes the attribution signal.

## E.2 Reference-Path Bias

**Definition E.1** (Path-induced attribution gap). Let  $R_a$  and  $R_b$  be two reference objectives with corresponding trajectories  $\theta_t^{(a)}$  and  $\theta_t^{(b)}$ . For a candidate  $z$ , the path-induced attribution gap is:

$$\Gamma_T(z; R, R_a, R_b) := \mathcal{I}_{R,R_a}^T(z) - \mathcal{I}_{R,R_b}^T(z). \quad (21)$$

**Remark:** This gap formalizes *reference-path bias*. If a pool-induced path ( $R_0 = R_{\text{pool}}$ ) differs geometrically from the target distribution, it moves the model through regions where the target gradient is weak or dominated by pool-specific noise. TACS corrects this by anchoring the path to the target proxy ( $R_0 = R_{\text{val}}$ ), ensuring candidates are scored in parameter regions actively shaped by the target signal.

## E.3 Extension to Adaptive Optimizers

This structural path dependence persists under adaptive optimizers (e.g., Adam). In the small-step limit, Adam induces a preconditioned flow  $\frac{d\theta_t}{dt} = -\eta_t P_t^{-1} \tilde{\nabla} R_0(\theta_t)$ , yielding the score:

$$\mathcal{I}_{R,R_0,\text{opt}}^T(z) := \int_0^T \eta_t \langle \nabla R(\theta_t), \tilde{g}(z, \theta_t) \rangle dt, \quad (22)$$

where  $\tilde{g}$  denotes the optimizer-transformed candidate direction, including both moment smoothing and the current preconditioner  $P_t^{-1}$ . Thus the displayed score should be read as the optimizer-aware analogue of the gradient inner product, not as an unpreconditioned candidate gradient. While the optimizer warps the local geometry, the fundamental dependence on the trajectory induced by  $R_0$  remains intact.

## E.4 Connection to Classical Influence Functions

We now demonstrate that finite-time path dependence reduces to the classical influence function *only* in a long-time equilibrium limit. Let  $L(\theta; w) := \sum_{j=1}^n w_j \ell(\theta; z_j)$  be a weighted objective, with gradient flow  $\frac{d\theta_t}{dt} = -\eta_t \nabla_{\theta} L(\theta_t; w)$ . We define the trajectory sensitivity as  $v_t := \frac{\partial \theta_t}{\partial w_i}$ .

**Lemma E.2** (Finite-time sensitivity equation). Assuming  $L$  is twice continuously differentiable,  $v_t$  satisfies:

$$\frac{d}{dt} v_t = -\eta_t H_t v_t - \eta_t \nabla_{\theta} \ell(\theta_t; z_i), \quad v_0 = 0, \quad (23)$$

where  $H_t := \nabla_{\theta}^2 L(\theta_t; w)$ .

*Proof.* Differentiating the gradient flow with respect to  $w_i$  and applying the chain rule to  $\nabla_{\theta} L(\theta_t; w)$  yields the result. Since  $\theta_0$  is independent of  $w_i$ ,  $v_0 = 0$ .  $\square$

**Lemma E.3** (Variation-of-constants representation). Let  $\Phi(t, s)$  be the state-transition operator for the homogeneous equation  $\frac{\partial}{\partial t} \Phi(t, s) = -\eta_t H_t \Phi(t, s)$  with  $\Phi(s, s) = I$ . The finite-time sensitivity is:

$$v_T = - \int_0^T \Phi(T, s) \eta_s \nabla_{\theta} \ell(\theta_s; z_i) ds. \quad (24)$$

**Remark on Path-Dependent Transport:** Lemma E.3 proves that a perturbation injected by candidate  $z_i$  at time  $s$  is transported to time  $T$  by  $\Phi(T, s)$ , which depends entirely on the Hessian field *along the specific reference trajectory*. Consequently, a path driven by a noisy candidate pool will inherently transport the attribution signal through irrelevant subspace directions, corrupting the final score.

**Proposition E.1** (Classical influence as the equilibrium limit). Suppose the flow converges to a stationary point  $\theta^*$ ,  $H := \nabla_{\theta}^2 L(\theta^*; w)$  is positive definite, and  $\int_0^{\infty} \eta_t dt = \infty$ . Then:

$$\lim_{T \rightarrow \infty} v_T = -H^{-1} \nabla_{\theta} \ell(\theta^*; z_i). \quad (25)$$

This matches the classical influence of upweighting  $z_i$  at  $\theta^*$ .

*Proof.* Near  $\theta^*$ ,  $H_t \rightarrow H$ . Under the time change  $\tau(t) = \int_0^t \eta_s ds$ , the asymptotic dynamics become  $\frac{d}{d\tau} v_{\tau} = -H v_{\tau} - \nabla_{\theta} \ell(\theta^*; z_i)$ . Since  $H \succ 0$ , this linear system has the unique stable equilibrium  $v_{\infty} = -H^{-1} \nabla_{\theta} \ell(\theta^*; z_i)$ , which is exactly the first-order condition of the perturbed minimizer.  $\square$

**Discussion: Equilibrium vs. Early Stopping in Modern LLMs.** Proposition E.1 establishes that if models were trained to strict convergence ( $t \rightarrow \infty$ ), the choice of optimization path would theoretically vanish, leaving only the local geometry of the optimum. However, modern deep learning—particularly LLM instruction-tuning—operates strictly in the finite-time, early-stopping regime. Because the path-independent limit in Eq. (25) is never reached, the sensitivity remains heavily path-dependent through the operators  $\Phi(T, s)$ . This formalizes the necessity of TACS: since attribution is inextricably linked to the finite-time integration path, that path must be explicitly conditioned on the target task ( $R_0 = R_{\text{val}}$ ) to isolate useful geometry.

## E.5 Proof of Theorem 6.1

We state a formal version of the cross-distribution transfer bound. Let  $P$  denote the target distribution and  $P'$  denote the selected-subset distribution.

**Theorem E.1** (Formal Wasserstein Cross-Distribution Risk Bound). Let  $\theta_P^*$  and  $\theta_{P'}^*$  be minimizers of  $R_P$  and  $R_{P'}$ , respectively. Assume that on a neighborhood containing  $\theta_0$ ,  $\theta_P^*$ , and  $\theta_{P'}^*$ : (i)  $R_P$  is  $\lambda$ -strongly convex and  $\beta$ -smooth; (ii) for every fixed  $\theta$ , the loss  $\ell(\theta; z)$  is  $L$ -Lipschitz in  $z$ ; and (iii) for every fixed  $\theta$ , the gradient  $\nabla_{\theta} \ell(\theta; z)$  is  $G$ -Lipschitz in  $z$ . Define the inverse transfer signal

$$\Delta := R_{P'}(\theta_0) - R_{P'}(\theta_P^*) > 0. \quad (26)$$

Then

$$R_P(\theta_0) - R_P(\theta_{P'}^*) \geq \Delta - 2LW_1(P, P') - \frac{\beta G^2}{2\lambda^2} W_1(P, P')^2. \quad (27)$$

In particular, when  $W_1(P, P')$  is small, the reverse target-task improvement is lower bounded by the inverse loss reduction  $\Delta$ , up to a Wasserstein distribution-shift penalty.

*Proof.* We first relate the target improvement toward  $\theta_P^*$  to the inverse transfer signal  $\Delta$ . By adding and subtracting risks under  $P'$ , we have

$$R_P(\theta_0) - R_P(\theta_P^*) = \Delta + [R_P(\theta_0) - R_{P'}(\theta_0)] - [R_P(\theta_P^*) - R_{P'}(\theta_P^*)]. \quad (28)$$

Since  $\ell(\theta; z)$  is  $L$ -Lipschitz in  $z$ , the Kantorovich–Rubinstein duality implies that, for any fixed  $\theta$ ,

$$|R_P(\theta) - R_{P'}(\theta)| \leq LW_1(P, P'). \quad (29)$$

Therefore,

$$R_P(\theta_0) - R_P(\theta_P^*) \geq \Delta - 2LW_1(P, P'). \quad (30)$$

It remains to account for the optimizer mismatch between  $\theta_P^*$  and  $\theta_{P'}^*$ . Since  $\nabla R_{P'}(\theta_{P'}^*) = 0$ ,

$$\|\nabla R_P(\theta_{P'}^*)\|_2 = \|\nabla R_P(\theta_{P'}^*) - \nabla R_{P'}(\theta_{P'}^*)\|_2 \quad (31)$$

$$\leq GW_1(P, P'), \quad (32)$$

where the last step again follows from Kantorovich–Rubinstein duality applied to the  $G$ -Lipschitz map  $z \mapsto \nabla_{\theta} \ell(\theta; z)$ . By  $\lambda$ -strong convexity of  $R_P$ ,

$$\|\theta_{P'}^* - \theta_P^*\|_2 \leq \frac{1}{\lambda} \|\nabla R_P(\theta_{P'}^*)\|_2 \leq \frac{G}{\lambda} W_1(P, P'). \quad (33)$$

Using  $\beta$ -smoothness of  $R_P$  and  $\nabla R_P(\theta_P^*) = 0$ ,

$$R_P(\theta_{P'}^*) - R_P(\theta_P^*) \leq \frac{\beta}{2} \|\theta_{P'}^* - \theta_P^*\|_2^2 \leq \frac{\beta G^2}{2\lambda^2} W_1(P, P')^2. \quad (34)$$

Finally,

$$R_P(\theta_0) - R_P(\theta_{P'}^*) = [R_P(\theta_0) - R_P(\theta_P^*)] - [R_P(\theta_{P'}^*) - R_P(\theta_P^*)]. \quad (35)$$

Substituting the two bounds above yields the claim.  $\square$

## F Experimental Details

### F.1 Controlled Logistic Regression Details

We use logistic-regression experiments [7] to isolate the geometry of target-conditioned data selection from the engineering details of instruction tuning. For a parameter vector  $\theta \in \mathbb{R}^d$ , examples are drawn from

$$x \sim \mathcal{N}(0, I_d), \quad \Pr(y = 1 \mid x) = \sigma(\langle x, \theta \rangle), \quad \sigma(t) = \frac{1}{1 + \exp(-t)}.$$

The selector observes the pool labels and a small target validation set; final performance is measured on an independent target-distribution test set. All trajectories are produced by full-batch gradient descent with a linearly-decaying learning rate. After selection, each method retrains a fresh logistic model from the same initialization on its selected subset.

**Training grids.** Pool, validation, and retraining trajectories share the same optimizer family. We sweep step counts in  $\{20, 40, 80, 160\}$  and base learning rates in  $\{0.3, 0.5, 0.7\}$ ; the validation-induced trajectory uses an additional learning-rate multiplier in  $\{0.5, 1.0, 2.0\}$ . Selection budgets cover a logarithmic grid up to the pool size.

**Balanced mixture.** The candidate pool contains equal mass from a target direction  $\theta^*$  and an orthogonal distractor direction  $\theta'$ ; validation and test data are drawn from  $\mathcal{P}_{\theta^*}$ . We use  $d = 10$ , a pool of order  $10^5$  examples, a validation set of order  $10^3$ , and a target-distribution test set of order  $10^4$ .

**Rare-target stress test.** Same logistic family with scarce target support: only 5% of the pool is drawn from  $\mathcal{P}_{\theta^*}$  and the remainder from distractor environments. We use  $d = 48$ , a small target validation set of order  $10^1$  examples, and a fixed selection budget  $k = 400$ . Target-source precision measures whether a selector recovers examples from the scarce target-support component; downstream target accuracy measures whether the selected subset improves the final model. Figure 6 reports the budget trend for both settings; at the table-equivalent endpoints ( $n = 8192$  balanced,  $k = 400$  rare), the selected-set recovery diagnostics are 63.8% target-source fraction for TACS vs. 50.1% for Random in the balanced setting, and target-source precision  $0.289 \pm 0.087$  (TACS) vs.  $0.179 \pm 0.069$  (LESS),  $0.156 \pm 0.060$  (ToV),  $0.044 \pm 0.011$  (Random) in the rare-target setting.

#### F.1.1 Trajectory Projection and Shape Distance

Figure 2 summarizes how the selected-subset retraining trajectory relates to the validation-induced and pool-induced reference paths. Let  $\theta_{0:T}^{(r)}$ ,  $\theta_{0:T}^{(v)}$ , and  $\theta_{0:T}^{(b)}$  denote the retraining, validation-induced, and pool-induced trajectories.

For Figure 2a we project only the final endpoint displacements onto a two-dimensional basis  $(e_1, e_2)$  given by the retraining displacement and the orthogonal component of the validation displacement:

$$e_1 = \frac{\theta_T^{(r)} - \theta_0^{(r)}}{\|\theta_T^{(r)} - \theta_0^{(r)}\|_2}, \quad e_2 = \frac{u}{\|u\|_2}, \quad u = \theta_T^{(v)} - \theta_0^{(v)} - \langle \theta_T^{(v)} - \theta_0^{(v)}, e_1 \rangle e_1.$$

Projection is for visualization only; scoring and retraining run in the original parameter space. Panel (a) should therefore be read as an endpoint-direction summary, not as a checkpoint-level trajectory plot. Each segment starts at the shared initialization and ends at the normalized final displacement of one trajectory. The basis  $(e_1, e_2)$  is computed *post hoc* from the final retraining and validation

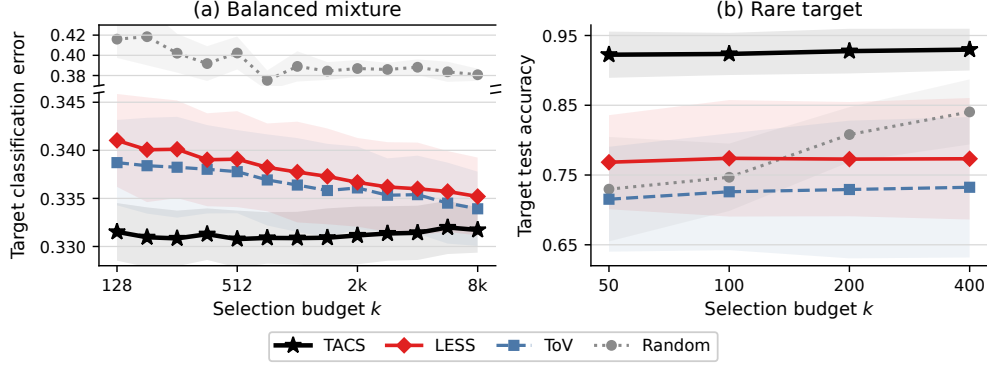


Figure 6: Controlled logistic-regression metrics across budgets, mean  $\pm$  std over 10 seeds. **(a)** Balanced mixture target error (lower better; broken y-axis). **(b)** Rare-target accuracy (higher better).

displacements so that their endpoint directions are visible in a common plane. Intermediate bending, curvature, and checkpoint spacing are intentionally not shown in panel (a); these are evaluated by the shape-distance diagnostic in Figure 2b, which is computed in the original  $\mathbb{R}^d$ .

For Figure 2b we compare trajectory shapes after normalizing path length. For  $\Theta = \{\theta_t\}$ ,  $\Phi = \{\phi_t\}$ , let  $\bar{\theta}_t = (\theta_t - \theta_0) / \|\theta_T - \theta_0\|_2$  (and similarly for  $\bar{\phi}_t$ ); the shape distance is defined as the average checkpoint-wise distance

$$d(\Theta, \Phi) := (T + 1)^{-1} \sum_{t=0}^T \|\bar{\theta}_t - \bar{\phi}_t\|_2.$$

The reported shape-distance ratio is

$$\frac{d(\theta^{(v)}, \theta^{(r)})}{d(\theta^{(b)}, \theta^{(r)})},$$

values below one mean the retraining path is closer in shape to the validation-induced path than to the pool-induced one. This diagnostic is not used by the selection algorithm.

## F.1.2 Scoring Protocol

TACS scores each candidate by normalized loss reduction along the validation-induced trajectory,

$$s_i^{\text{TACS}} = \frac{\ell_i(\theta_{\text{ref}}) - \ell_i(\theta_{\text{last}})}{\max\{\ell_i(\theta_{\text{ref}}), \varepsilon\}},$$

where  $\theta_{\text{ref}}$  is the first validation checkpoint and  $\theta_{\text{last}}$  the last. The validation-warmup length and learning-rate multiplier are tuned by a small held-out proxy-vs-negative-reference AUROC search over the grids in the previous paragraph, using the same calibration protocol as Appendix F.6.

For the logistic baselines, we use controlled analogues of LESS and ToV rather than the original instruction-tuning implementations. They are customized to the logistic-regression setting so that all dynamic selectors share the same candidate-pool warmup checkpoints  $\{\theta_t^{\text{pool}}\}_{t \in \mathcal{K}}$ , optimizer grid, validation set, selection budget, and downstream retraining protocol. LESS uses the finite-dimensional analogue of trajectory-gradient matching:

$$s_i^{\text{LESS}} = |\mathcal{K}|^{-1} \sum_{t \in \mathcal{K}} \left\langle \nabla_{\theta} \ell(\theta_t^{\text{pool}}; z_i), \nabla_{\theta} R_{\text{val}}(\theta_t^{\text{pool}}) \right\rangle.$$

ToV perturbs each pool checkpoint by one short validation update,  $\theta_t^{\text{tov}} = \theta_t^{\text{pool}} - \alpha \eta_t \nabla_{\theta} R_{\text{val}}(\theta_t^{\text{pool}})$ , and averages the candidate improvement

$$s_i^{\text{ToV}} = |\mathcal{K}|^{-1} \sum_{t \in \mathcal{K}} [\ell(\theta_t^{\text{pool}}; z_i) - \ell(\theta_t^{\text{tov}}; z_i)].$$

We tune the ToV perturbation multiplier  $\alpha$  over the same multiplier grid used for validation-induced calibration. Thus the logistic comparison isolates the reference-path and scoring-direction choice: all three dynamic selectors use matched optimizers, checkpoint budgets, validation data, and downstream retraining.

## F.2 Details for Computer Vision Runs

**Setup.** The computer-vision experiments test whether validation-induced scoring transfers outside instruction tuning. We use CIFAR-10 [24] with an ImageNet-pretrained [8] ResNet-18 backbone [15]. The target task is binary CIFAR-10 cat-vs-dog classification with a 100-image clean validation proxy and a held-out clean target-distribution test split. The candidate pool contains 10,000 CIFAR-10 training images drawn from all classes, so target-class examples are mixed with semantically unrelated distractors. Non-target classes are included as distractors during selection; downstream accuracy is evaluated on the cat-vs-dog target split. In the noisy condition, labels for 40% of the pool are randomly corrupted before selection and retraining; validation and test labels remain clean.

**Methods.** We compare TACS with random selection, LESS [49], GraNd, EL2N [32], and Embedding Retrieval. The LESS and ToV-style vision baselines are task-matched analogues customized for this CIFAR-10 setting, not the original instruction-tuning benchmark configurations. TACS fine-tunes the backbone on the validation proxy and scores each pool image by normalized endpoint loss reduction. LESS computes validation-pool gradient similarity along a short candidate-pool warmup. GraNd and EL2N score by early-training gradient norm and error  $L_2$ -norm. Embedding Retrieval ranks pool images by cosine similarity between pretrained-backbone features and the mean validation embedding. All methods use the same pool, selection budget, preprocessing, and downstream retraining protocol.

**Training grids.** All trainable stages use Adam. Selection budgets are  $k \in \{100, 250, 500, 1000\}$ . Downstream retraining (and any method-internal warmup) sweeps the learning rate in  $\{10^{-5}, 5 \times 10^{-5}, 10^{-4}, 5 \times 10^{-4}\}$  and the number of epochs in  $\{2, 4, 8, 16\}$ , with mini-batch sizes in  $\{32, 64, 128\}$ . For ToV the validation-perturbation phase additionally uses a learning-rate multiplier in  $\{0.1, 0.3, 1.0\}$  over the base-warmup learning rate. Per-method choices within these grids are calibrated on a small held-out split of the validation proxy.

**Evaluation.** Each method retrains on its selected subset and is evaluated on the clean held-out target split. We report target accuracy, selected clean-label fraction, and selected target-class fraction, which separate label-corruption and off-target failure modes. “Full fine-tuning” updates all ResNet-18 parameters; “partial fine-tuning” updates the final residual block and classification head. Clean-pool full-fine-tuning uses 5 seeds to reduce variance in the non-corrupted reference setting, while the noisier robustness setting uses 3 seeds because each run includes the additional corrupted-pool construction and diagnostics.

At  $k = 500$  under full fine-tuning, LESS obtains higher accuracy than TACS in the clean candidate pool ( $80.48 \pm 2.19\%$  versus  $71.79 \pm 10.59\%$ ). Under 40% label noise, however, LESS degrades to  $57.68 \pm 3.93\%$ , while TACS reaches  $77.35 \pm 2.36\%$ . The selected-set diagnostics mirror this reversal: in the noisy pool, TACS selects 79.9% clean-label examples and 83.5% target-distribution examples, compared with 40.7% and 45.2% for LESS.

**Interpreting the Noisy-Pool Comparison.** The clean/noisy comparison is a robustness diagnostic, not evidence that label noise is beneficial. TACS scores come from a validation-induced trajectory independent of the candidate pool; differences arise after truncating the ranked list at budget  $k$  and retraining on that subset. At small budgets, a clean pool can concentrate on a narrow high-alignment mode, whereas the noisy pool pushes corrupted and off-target examples into the negative tail and can leave a more spread-out clean target-class subset. This effect is budget-limited: by  $k = 1000$ , clean full-fine-tuning again exceeds noisy full-fine-tuning ( $78.1\%$  versus  $75.7\%$ ). A direct fix for the small-budget clean-pool case would be diversity or deduplication re-ranking on top of TACS scores.

**Trends.** Figure 7 expands the main-text  $k = 500$  slice across budgets and pools. Under full fine-tuning, TACS and LESS are the strongest methods at moderate and large budgets; generic difficulty scores (GraNd, EL2N) remain weaker because they are not conditioned on the target proxy. The noisy-pool panels are the most diagnostic: TACS retains high target accuracy under 40% label corruption, while LESS degrades; the corresponding clean-label and target-distribution fractions of the selected subsets move in the same direction, supporting the interpretation that the validation-induced trajectory acts as a task-conditioned filter rather than a generic difficulty score.

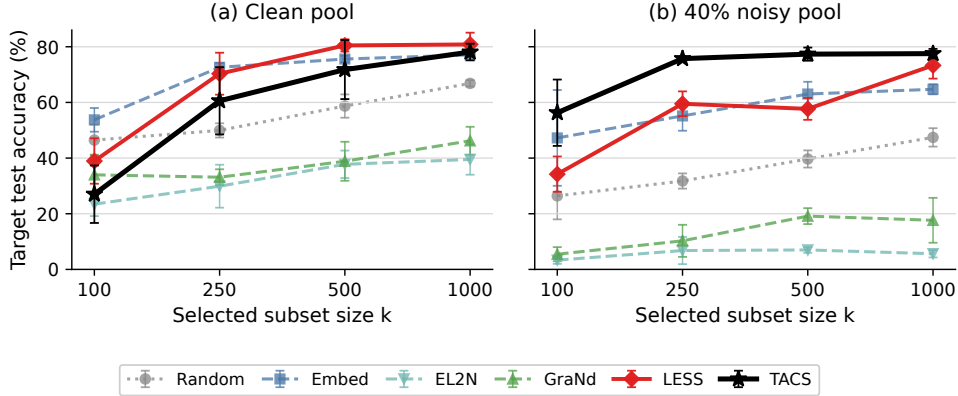


Figure 7: Binary CIFAR-10 target accuracy across budgets under clean and 40% noisy pools. Full fine-tuning updates all ResNet-18 parameters.

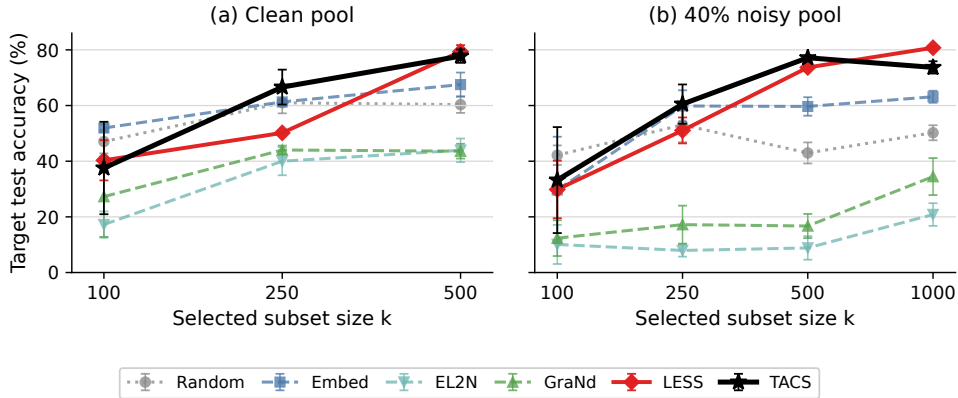


Figure 8: Binary CIFAR-10 partial fine-tuning: only layer4 and the classification head are retrained after selection.

Figure 8 repeats the budget sweep with a restricted downstream learner: only the final residual block and classification head are retrained after selection. The same broad ordering persists, with TACS and LESS separated from random selection and generic data-pruning metrics at larger budgets. This suggests that the selected examples carry target-relevant information even when downstream retraining has limited capacity to compensate for poor selection.

### F.3 Details for Instruction Tuning

In this section, we provide the comprehensive implementation details, dataset statistics, and hyperparameter configurations omitted from the main text for the instruction tuning experiments (Section 5.2).

#### F.3.1 Dataset

Table 4 details the sizes and formats of the candidate pools and target development sets used in our cross-distribution evaluation. We utilize standard splits for all datasets. Our candidate pools consist of four widely used instruction tuning collections: Flan V2 [26] (licensed under Apache 2.0), Oasst1 [23] (Apache 2.0), COT [47] (MIT License), and Dolly [6] (CC BY-SA 3.0). For downstream evaluation and target proxies, we employ MMLU [16] (MIT License) for general knowledge, BBH [37] (MIT License) for complex reasoning, and TyDiQA [5] (Apache 2.0) for multilingual question answering. To maintain structural consistency across all diverse sources and tasks listed in Table 4, every example is compiled into the standard Tulu chat format [45] prior to tokenization and training.

Table 4: Dataset statistics for candidate training pools ( $\mathcal{Z}$ ) and target task development sets ( $\mathcal{Z}_{\text{val}}$ ).

Candidate Pools		Target Dev Sets		
Source	Size	Task	Size	Format
flan_v2	100,000	mmlu	285	(5-shot)
cot	100,000	bbh	81	(1-shot)
oasst1	55,668	tydiqa	9	(1-shot)
dolly	15,011			

Table 5: Standardized Tulu format template used for compiling all dataset examples.

Tulu Chat Format
< system >
A chat between a curious user and an artificial intelligence assistant...
< user >
{Instruction / Context / Prompt}
< assistant >
{Target Response}

### F.3.2 Model and Training Configurations

For all experiments, we use the Llama-3.2-3B foundation model (released under the Llama 3.2 Community License) [11]. For standard downstream retraining and candidate pool warmups (used by baselines), we apply Low-Rank Adaptation (LoRA) to the base model with a rank of  $r = 128$  and a scaling factor of  $\alpha = 512$ . These downstream retraining and candidate-pool warmup runs use AdamW (adamw\_torch) with weight decay 0.0. In contrast, for the main cross-candidate-source results table, the TACS validation-induced warmup uses a restricted capacity bottleneck with  $r = 1$  and  $\alpha = 4$ , also optimized with AdamW and weight decay 0.0. As analyzed in the ablation study, this ultra-low rank acts as a structural regularizer to improve the stability of TACS on small validation sets and makes validation-induced warmup trajectories cheap to store offline for reuse.

### F.3.3 Baseline Implementations

We compare our method against LESS [49] and ToV [18]. The definitions below apply to the instruction-tuning experiments; the controlled logistic-regression and CIFAR-10 experiments use matched analogues described in their respective sections rather than the original LESS/ToV benchmark settings.

- For **LESS**, we follow the authors’ official implementation for gradient projection (dimension  $d_{\text{proj}} = 8192$ ). Let  $m_i^{(t)}$  denote the Adam-moment candidate gradient representation for candidate  $z_i$  at checkpoint  $t$ ,  $g_{\text{val}}^{(t)}$  the validation gradient representation, and  $P_t$  the random projection. We score by aggregated projected cosine similarity:

$$s_i^{\text{LESS}} = |\mathcal{K}|^{-1} \sum_{t \in \mathcal{K}} \frac{\langle P_t m_i^{(t)}, P_t g_{\text{val}}^{(t)} \rangle}{\|P_t m_i^{(t)}\|_2 \|P_t g_{\text{val}}^{(t)}\|_2}.$$

During warmup, the model is trained on a randomly selected subset of the corresponding data pool with the same size as the selection budget for 4 epochs.

- For **ToV**, we implement method A and the “Maximum-Improvement” rule from the ToV paper. For each base checkpoint  $\theta_t$ , we perturb on the target validation proxy to obtain  $\theta'_t$ . Candidate  $z_i$  is scored by the largest raw candidate-loss improvement across perturbation checkpoints:

$$s_i^{\text{ToV}} = \max_{t \in \mathcal{K}} [\ell(\theta_t; z_i) - \ell(\theta'_t; z_i)].$$

Following their methodology, the perturbation learning rate is  $0.1 \times$  the base learning rate for stability.

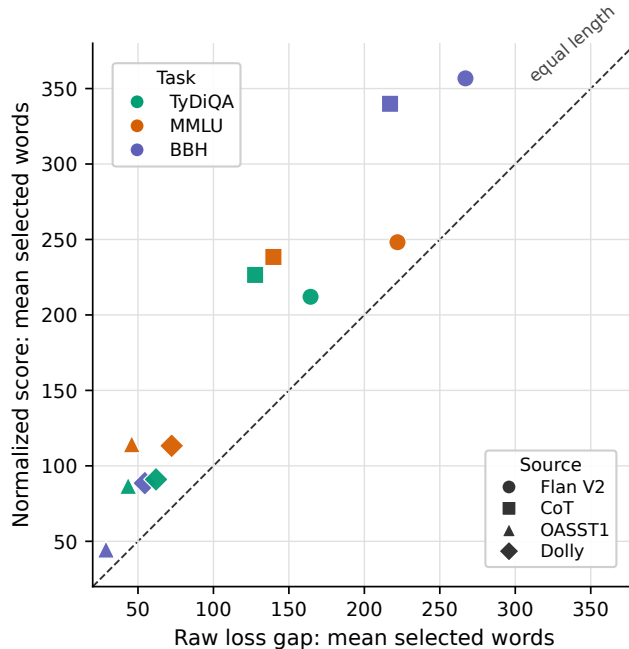


Figure 9: First-loss normalization vs. selected-example length. Each point is one task-source cell, with color indicating the target task and marker shape indicating the candidate source. Points above the diagonal mean normalization selects longer examples.

### F.3.4 Evaluation Protocol and Hardware

In all experiments, we fix the selection budget to 5% of the respective candidate pool size. Final results are evaluated on the standard held-out test sets of MMLU, BBH, and TyDiQA. All reported metrics are averaged across 3 independent random seeds. All experiments, including warmup, scoring, and retraining, were conducted on a single NVIDIA H200 GPU.

## F.4 Ablation Study

### F.4.1 Length Normalization and Selected-Example Length

Instruction-tuning examples vary substantially in output length, so raw loss-drop scores can be confounded by scale. We therefore diagnose the effect of the normalized TACS score

$$s(z) = \frac{\ell(\theta_1; z) - \ell(\theta_T; z)}{\max\{\ell(\theta_1; z), \varepsilon\}}$$

against the unnormalized loss gap  $\ell(\theta_1; z) - \ell(\theta_T; z)$ . The diagnostic uses the paper-facing Llama-3.2-3B sourcewise TACS benchmark and compares the top-5% selected set for every task-source cell.

Figure 9 shows that first-loss normalization does not create a short-example bias. In all 12 task-source cells, normalized scoring selects longer examples on average than raw loss-gap scoring. The average increase in selected mean length is +59.6 words, with median increase +45.5 words. The selected sets also change substantially: raw-vs-normalized overlap ranges from 30.6% to 71.4%. The largest mean-length shifts occur for BBH/COT (+122.9 words), MMLU/COT (+98.7 words), and TyDiQA/COT (+98.9 words). This supports using first-loss normalization in the main experiments: it changes the ranking materially while avoiding the tendency of raw loss gaps to favor short, high-variance examples.

Figure 10 gives the corresponding distributional view. The pool length distributions are strongly right-skewed, so raw endpoint loss gaps can be dominated by scale effects from unusually short or long examples depending on the source. Normalization does not collapse selection to a narrow

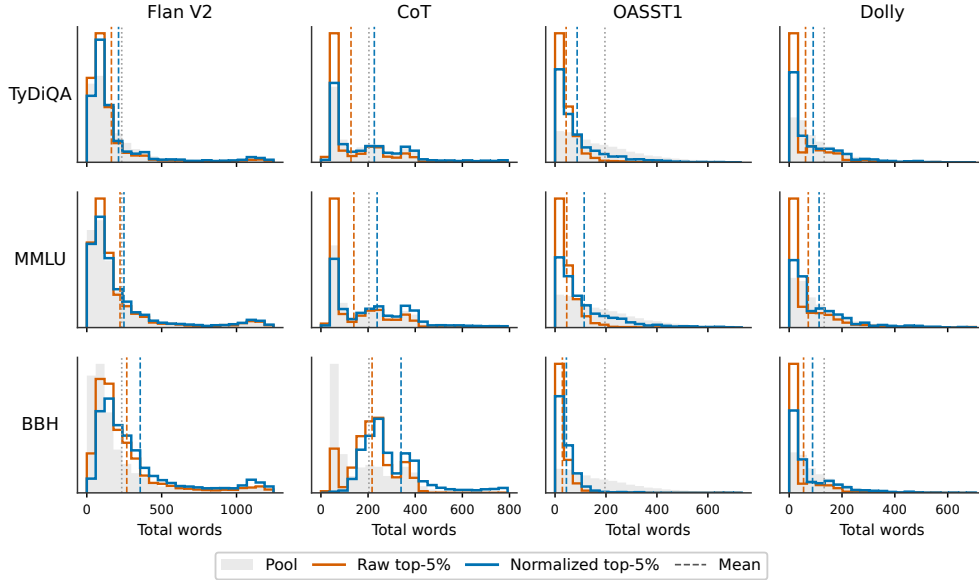


Figure 10: Selected-length distributions under raw and normalized endpoint loss gaps. Gray histograms show the full pool, colored curves show selected top-5% subsets, and dashed vertical lines mark means.

length band: the normalized top-5% generally remains spread over the support of the pool and often shifts the selected mean to the right of the raw-loss selection. This supports the use of relative loss reduction as a length-stabilized score rather than as a hidden preference for short outputs.

## F.5 Score Variant Ablation

The normalized endpoint score in Eq. (16) is motivated primarily by instruction-tuning settings, where examples may differ in length, format, and initial loss scale. Since TACS is not specific to LLMs, we also test in our controlled prediction settings how two engineering choices in the score definition affect selection performance: (i) normalizing the endpoint loss drop, and (ii) using  $\theta_1^{\text{val}}$  rather than  $\theta_0^{\text{val}}$  as the baseline checkpoint. The main TACS score corresponds to the normalized  $\theta_1^{\text{val}} \rightarrow \theta_T^{\text{val}}$  variant.

We compare four score variants: raw and normalized endpoint loss drops, each computed either from  $\theta_0^{\text{val}}$  or from  $\theta_1^{\text{val}}$ . Concretely, for  $a \in \{0, 1\}$ ,

$$s_a^{\text{raw}}(z) = \ell(\theta_a^{\text{val}}; z) - \ell(\theta_T^{\text{val}}; z), \quad s_a^{\text{norm}}(z) = \frac{\ell(\theta_a^{\text{val}}; z) - \ell(\theta_T^{\text{val}}; z)}{\max\{\ell(\theta_a^{\text{val}}; z), \varepsilon\}}.$$

The main score is  $s_1^{\text{norm}}$ . In the logistic-mixture setting, all four variants are nearly identical: they produce the same ranking diagnostics, almost the same top- $k$  target fractions, and indistinguishable downstream classification error. This indicates that, in the controlled convex setting, the TACS signal is not an artifact of normalization or of dropping the first checkpoint.

In noisy CIFAR-10, normalization has a clearer practical effect. Figure 11 shows that normalized scores select substantially higher fractions of target-class and clean-label examples, especially at small budgets. For example, at  $k = 100$ , the target-class fraction improves from 0.623 to 0.810 when using normalization with the  $\theta_0^{\text{val}} \rightarrow \theta_T^{\text{val}}$  score, and from 0.553 to 0.810 for the corresponding  $\theta_1^{\text{val}}$ -based score. By contrast, replacing  $\theta_0^{\text{val}}$  with  $\theta_1^{\text{val}}$  has a smaller empirical effect. Overall, these results suggest that normalization is the practically important correction in the noisy neural setting, while dropping  $\theta_0^{\text{val}}$  is a mild and conservative stabilization choice.

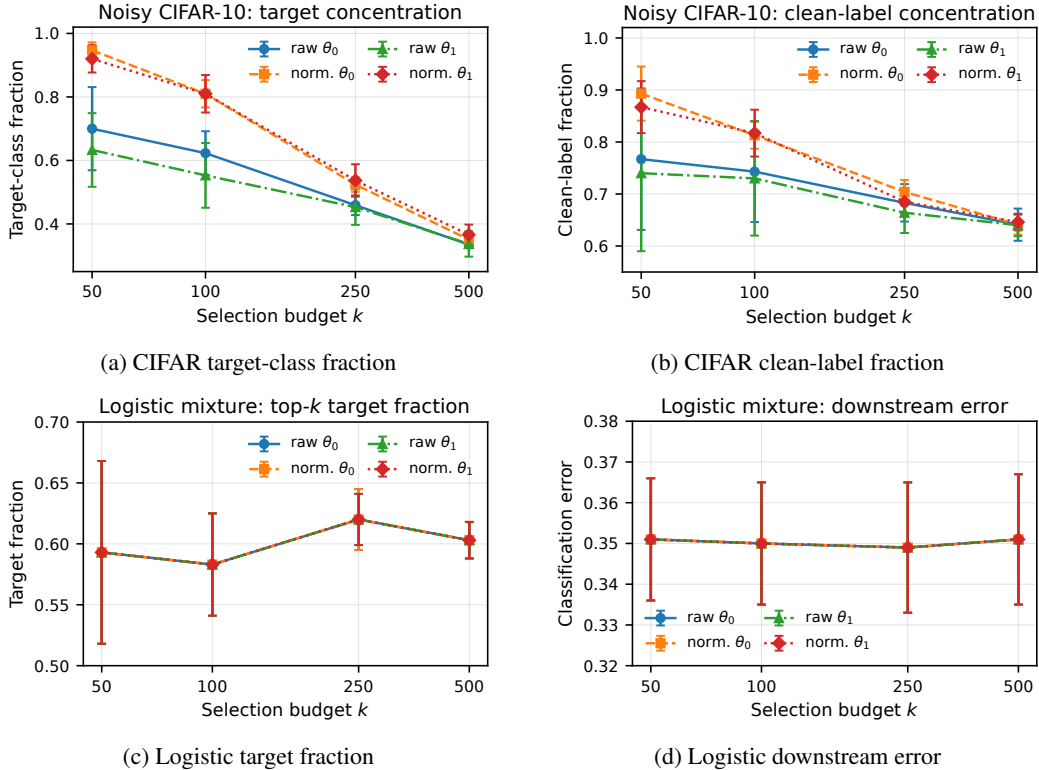


Figure 11: Score-variant ablation in noisy CIFAR-10 and logistic regression. In CIFAR-10, normalization substantially improves target-class and clean-label concentration, especially at small selection budgets. In logistic regression, all four variants are nearly indistinguishable, indicating that the TACS signal in the controlled convex setting is not an artifact of normalization or first-checkpoint removal.

## F.6 Hyperparameter Selection via M-Fold Cross-Validation

To automate the selection of the two key target-conditioned warmup hyperparameters—learning rate ( $\eta$ ) and total training epochs ( $T$ )—we implement a standard  $M$ -fold cross-validation procedure [36, 22]. Crucially, to maintain the  $\mathcal{O}(1)$  computational efficiency of TACS, we utilize an ultra-low capacity LoRA adapter ( $r = 1, \alpha = 4$ ) for all calibration runs. This is a small one-time calibration cost: in our Llama-3.2-3B implementation, Table 2 reports 1.2 H200 GPU hours for calibration, after which the selected trajectory can be reused under the same target, base model, and scoring setup.

We select  $\eta$  and  $T$  via a joint grid search over  $\eta \in \{2 \times 10^{-6}, 5 \times 10^{-6}, 2 \times 10^{-5}, 5 \times 10^{-5}, 2 \times 10^{-4}\}$  and  $T \in \{4, 8, 12, 16\}$  epochs. Our core intuition is that an optimal warmup trajectory should maximize the geometric separation between the target distribution and a generic negative reference sample.

### F.6.1 Probing Set Construction

We employ an  $M$ -fold cross-validation strategy ( $M = 3$ ) on the target validation proxy  $\mathcal{Z}_{\text{val}}$ . For each fold  $i$ , we partition  $\mathcal{Z}_{\text{val}}$  such that two-thirds form the active warmup set  $\mathcal{Z}_{\text{warmup}}^{(i)}$  and one-third serves as the held-out positive class  $S_{\text{target}}^{(i)}$ . To represent the negative class, we use a fixed generic reference sample  $S_{\text{neg}}$  with  $N_{\text{neg}} = 100$  examples. In our experiments this reference is sampled uniformly from the available uncured pool for convenience, but it need not be drawn from the candidate pool later being scored. The negative sample is used *only* for hyperparameter selection; final candidate ranking is recomputed over the entire uncured pool using a trajectory trained on the full  $\mathcal{Z}_{\text{val}}$ .

---

**Algorithm 2**  $M$ -Fold Trajectory Calibration

---

- 1: **Input:** Target validation set  $\mathcal{Z}_{\text{val}}$ , generic negative reference sample  $S_{\text{neg}}$
  - 2: **Search space:** learning-rate grid  $H_\eta$ , epoch grid  $H_T = \{4, 8, 12, 16\}$
  - 3: Partition  $\mathcal{Z}_{\text{val}}$  into  $M = 3$  folds
  - 4: **for** each learning rate  $\eta \in H_\eta$  **do**
  - 5:   **for** each fold  $i = 1, \dots, M$  **do**
  - 6:     Form warmup set  $\mathcal{Z}_{\text{warmup}}^{(i)}$  from the remaining folds and held-out positives  $S_{\text{target}}^{(i)}$
  - 7:     Train rank-one LoRA on  $\mathcal{Z}_{\text{warmup}}^{(i)}$  with learning rate  $\eta$  up to max  $H_T$  epochs
  - 8:     **for** each  $T \in H_T$  **do**
  - 9:       Extract  $\theta_1$  and  $\theta_T$
  - 10:       Compute normalized loss reduction for  $S_{\text{target}}^{(i)} \cup S_{\text{neg}}$
  - 11:       Compute AUROC $^{(i)}(\eta, T)$  separating target positives from reference negatives
  - 12:     **end for**
  - 13:   **end for**
  - 14:   Compute mean AUROC  $\bar{A}(\eta, T) = M^{-1} \sum_i \text{AUROC}^{(i)}(\eta, T)$
  - 15: **end for**
  - 16: **return**  $(\eta^*, T^*) = \arg \max_{\eta, T} \bar{A}(\eta, T)$
- 

### F.6.2 Optimization Objective

We quantify candidate utility via the Normalized Loss Reduction  $s(x) = (\ell(\theta_1; x) - \ell(\theta_T; x)) / \max\{\ell(\theta_1; x), \varepsilon\}$ . The objective is to maximize the average separation between the held-out target proxy  $S_{\text{target}}^{(i)}$  and the negative reference sample  $S_{\text{neg}}$ . For each fold  $i$ , we pool the scores for  $S_{\text{target}}^{(i)} \cup S_{\text{neg}}$  and calculate the AUROC using the Mann–Whitney rank formulation:

$$\text{AUROC}^{(i)}(\eta, T) = \frac{\sum_{x \in S_{\text{target}}^{(i)}} \text{rank}(s(x)) - |S_{\text{target}}^{(i)}|(|S_{\text{target}}^{(i)}| + 1)/2}{|S_{\text{target}}^{(i)}| |S_{\text{neg}}|} \quad (36)$$

where  $\text{rank}(\cdot)$  denotes the ascending rank of the scores in the joint set.

This calibration is intentionally heuristic. For very small target proxies, such as the 9-example TyDiQA development set, each three-fold held-out split contains only three positive examples, so the AUROC objective is discrete and can have high variance. We use it to choose a reasonable traversal scale, not as a statistically precise estimate of final downstream performance.

### F.6.3 Joint Grid Search Procedure

Optimizing  $\eta$  and  $T$  jointly identifies the optimal traversal speed through the target task’s *Structural Alignment Regime*. To optimize compute, we evaluate all epoch checkpoints  $T$  for a given learning rate within a single training run per fold. Once the optimal configuration  $(\eta^*, T^*)$  is identified by the highest mean AUROC across folds, we execute a single, final warmup trajectory using the entirety of  $\mathcal{Z}_{\text{val}}$  to score the downstream candidate pool.